Hubbard models for quasicrystalline potentials

E. Gottlob and U. Schneider*

Cavendish Laboratory, University of Cambridge, J. J. Thomson Avenue, Cambridge CB3 0HE, United Kingdom

(Received 15 November 2022; accepted 27 February 2023; published 10 April 2023)

Quasicrystals are long-range ordered, yet not periodic, and thereby present a fascinating challenge for condensed matter physics, as one cannot resort to the usual toolbox based on Bloch's theorem. Here, we present a numerical method for constructing the Hubbard Hamiltonian of nonperiodic potentials without making use of Bloch's theorem and apply it to the case of an eightfold rotationally symmetric two-dimensional optical quasicrystal that was recently realized using cold atoms. We construct maximally localized Wannier functions and use them to extract onsite energies, tunneling amplitudes, and interaction energies. In addition, we introduce a configuration-space representation, where sites are ordered in terms of shape and local environment, that leads to a compact description of the infinite-size quasicrystal in which all Hamiltonian parameters can be expressed as smooth functions. The configuration-space picture serves as an aperiodic analog of the Brillouin zone, and allows one to efficiently describe the quasicrystal in the thermodynamic limit, enabling new analytic arguments on the topological structure and many-body physics of these models. For instance, we use it to conclude that this quasicrystal will host unit-filling Mott insulators in the thermodynamic limit.

DOI: 10.1103/PhysRevB.107.144202

Quasicrystals represent a fascinating middle ground between periodic and disordered materials: they are perfectly long-range ordered without being periodic [1]. Quasicrystalline order can naturally arise from an incommensurate projection of a higher-dimensional periodic lattice and thereby enables the investigation of physics of higher dimensions, in particular in the context of topology [2–6], where the resulting structures can inherit topologically protected edge states [3,4,6]. Quasicrystals host fractal, self-similar structures both in momentum space [1] and in their energy spectrum [7]. They also exhibit Anderson localization [8], broadly similar to disordered systems. However, there are crucial differences: in randomly disordered systems in one and two dimensions (1D and 2D), the noninteracting spectrum is always fully localized [9]. Quasiperiodic systems, on the other hand, can host mobility edges and localization transitions at finite potential strengths [10–14]. In the interacting case, localization can subsist in the form of many-body localization, whose nonergodic nature has been the subject of significant attention over the last few years [15–19]. There is strong interest in the differences in many-body localization between quasiperiodic and disordered systems [20], in particular in more than one dimension, where avalanche effects are predicted to destabilize many-body localization in the latter case [21].

To study phase transitions and localization phenomena, it is convenient to describe the continuum lattice potential as a tight-binding model, i.e., as a collection of discrete lattice sites. This tremendously reduces the computational complexity of diagonalizing the Hamiltonian, and therefore allows for the study of far larger system sizes. The key step in constructing a tight-binding Hamiltonian is to generate a set of localized Wannier functions. In periodic lattices, these are constructed as an appropriate superposition of Bloch waves [22] which, however, do not exist for nonperiodic potentials. For general nonperiodic lattices, existing generic methods for calculating Wannier functions are based on imaginary-time evolution of trial wave functions [23], or rely on full band projections [24].

Constructing exact tight-binding models for general quasicrystals is difficult because (a) one cannot use Bloch's theorem to construct appropriate Wannier functions and (b) the lack of periodicity typically prevents one from efficiently describing their thermodynamic limit. Several quasiperiodic models, such as Aubry-André models [10,13,14,25–27], are explicitly constructed using quasiperiodic perturbations of an initially periodic lattice and thereby inherit the original Wannier functions. These models, however, represent only particular limits of general quasicrystalline potentials.

In this paper, we present a method for generating nonperiodic Hubbard Hamiltonians without using Bloch's theorem, and apply it to the two-dimensional eightfold rotationally symmetric optical quasicrystal (8QC) (see Fig. 2), which has recently been realized with ultracold atoms [28,29]. In addition, we introduce a configuration-space description of this quasicrystal, where sites are ordered according to their shape and local environment, which serves as an aperiodic analog of the Brillouin zone, and allows to describe the infinite-size quasicrystal in terms of smooth functions in a compact parameter space. This method is similar to configuration-space descriptions employed for stacked bilayer systems [30–32] and the resulting description directly corresponds to perpendicular spaces widely used in the field of discrete quasicrystals [33–37].

In Sec. I, we present a method for the generation of maximally localized Wannier functions that is applicable to a

*uws20@cam.ac.uk

broad class of quasicrystalline or disordered potentials. We then apply it in Sec. II to construct the lowest-band Hubbard Hamiltonian of the 8QC. In Sec. III, we address the description of the quasicrystal in the infinite-size limit. We show in Sec. III A how the 8QC Hubbard Hamiltonian is greatly simplified when reexpressed in configuration space. In Sec. III B, we discuss how the validity of the single-band picture is impacted by interparticle interactions. Finally, in Sec. III C, we use the insight gained from the configuration-space expression of the 8QC Hubbard Hamiltonian to conclude on the existence of unit-filling Mott-insulating phases in the thermodynamic limit.

I. TIGHT-BINDING MODEL FOR NONPERIODIC POTENTIALS

Let us consider a nonperiodic lattice described by the *continuum* single-particle Hamiltonian

$$\hat{H}_{\text{cont}} = \frac{\hat{p}^2}{2m} + \hat{V}(\mathbf{r}),$$

where $\hat{p}$ is the momentum operator, m the particle mass, and $\hat{V}(\mathbf{r})$ the nonperiodic lattice potential. To generate the tight-binding Hamiltonian, the key step is to obtain an appropriate set of localized single-particle basis states $\{|w_i\rangle\}$ on each site of the lattice, as represented in Fig. 1. We will refer to these states as Wannier functions, even though we are dealing with nonperiodic systems where Bloch's theorem does not apply. Our numerical method can be summarized as follows: First, nonorthogonal maximally localized Wannier functions (NOWF) are generated individually on each lattice site by minimizing the width of a linear combination of eigenstates of the potential (see below). Second, a Löwdin transformation is applied onto the resulting nonorthogonal set, producing a set of maximally localized and orthogonal Wannier functions (WF). If applied onto a periodic lattice, our method produces the same Wannier functions that would be obtained using the typical Bloch wave formalism.

After constructing the Wannier functions, we generate the Hubbard Hamiltonian (Fig. 1) in the usual way by the explicit evaluation of its matrix elements, namely, onsite energies $\epsilon_i = \langle w_i|\,\hat{H}_{\text{cont}}\,|w_i\rangle$, hopping amplitudes $J_{ij} = \langle w_i|\,\hat{H}_{\text{cont}}\,|w_j\rangle$, and onsite interactions $U_i = g\int d\mathbf{r}|w_i(\mathbf{r})|^4$, where $g = \frac{4\pi\hbar^2}{m}a$ and a is the scattering length of the considered atomic species. Off-site interactions can also be obtained through the evaluation of integrals involving neighboring Wannier functions (see Appendix E) [38].

Maximally localized Wannier functions in real-space formulation

Given the nonperiodicity of the lattice potential, we cannot rely on Bloch waves for the generation of WFs. Instead, we start by numerically calculating the single-particle eigenstates $|E_k\rangle$ of the continuum Hamiltonian in a domain of radius R centered around the lattice site at position $\mathbf{r}_i$. We can then express the localized NOWF $|w^{\text{NO}}\rangle$ as a linear combination of the single-particle eigenstates within the energy band of interest ($E_{\min} \leqslant E_k \leqslant E_{\max}$):

$$|w^{\text{NO}}\rangle = \sum_k c_k\,|E_k\rangle\,. \tag{1}$$

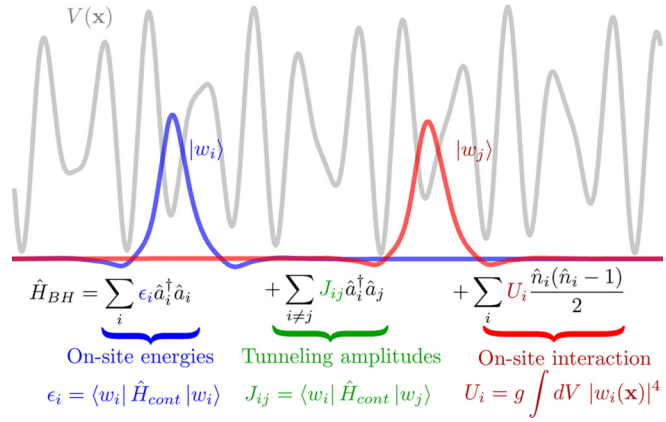

FIG. 1. Hubbard models are expressed in terms of onsite energies, tunneling amplitudes, and onsite interactions, which we compute by constructing maximally localized Wannier functions. In nonperiodic systems, all Wannier functions and therefore parameters are site dependent.

We note that, contrary to periodic crystals, the existence of band gaps separating individual bands is not guaranteed for nonperiodic potentials and must be checked individually for each specific lattice potential.

The coefficients c_k are determined by minimizing the localization criterion [22]

$$\Omega_i \equiv \langle w^{\text{NO}}|\,(\mathbf{r}-\mathbf{r}_i)^2\,|w^{\text{NO}}\rangle$$

subject to the normalization constraint $\sum_k |c_k|^2 = 1$. We can recast this expression as a double sum over all eigenstates $|E_k\rangle$:

$$\begin{aligned}\Omega_i &= \sum_{k,l} c_k^* c_l\,\langle E_k|\,(\mathbf{r}-\mathbf{r}_i)^2\,|E_l\rangle \\ &= \sum_{k,l} c_k^* c_l \big(R_i^2\big)_{kl} \\ &= \mathbf{c}^\dagger R_i^2 \mathbf{c},\end{aligned} \tag{2}$$

where we combine the coefficients c_k into the vector $\mathbf{c}$ and define the Hermitian and positive-definite matrix R_i^2 with matrix elements $(R_i^2)_{kl} = \langle E_k|\,(\mathbf{r}-\mathbf{r}_i)^2\,|E_l\rangle$.

$|w_i^{\text{NO}}\rangle$, i.e., the most localized state that can be generated on the lattice site $\mathbf{r}_i$, is then directly obtained as the eigenvector of (R_i^2) with the lowest eigenvalue (which is real valued thanks to Hermiticity). While being maximally localized, the resulting states $|w_i^{\text{NO}}\rangle$ on different sites will not yet be orthogonal.

To obtain an orthogonal set of localized basis states $|w_i\rangle$, the nonorthogonal basis must now be transformed in a way that maintains its localized properties. This is achieved through a Löwdin transformation [39]

$$|w_i\rangle = \sum_j S_{ij}^{-1/2}\,\big|w_j^{\text{NO}}\big\rangle, \tag{3}$$

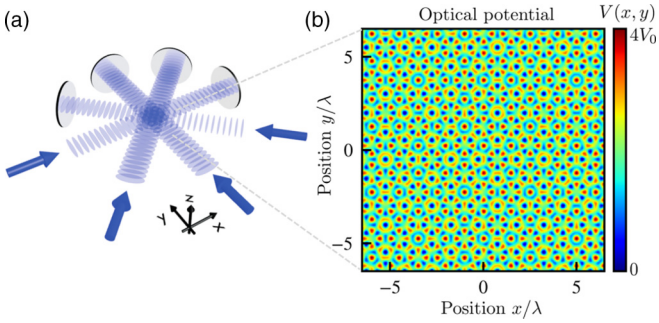

FIG. 2. Two-dimensional eightfold optical quasicrystal. (a) The optical quasicrystal is formed by superimposing two square optical lattices in a single plane with a 45° angle between them. (b) The resulting optical potential is quasiperiodic.

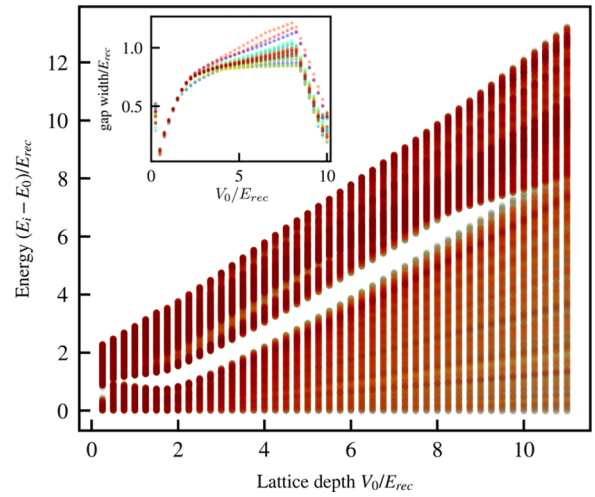

FIG. 3. Low-energy single-particle energy spectrum of the 8QC continuum Hamiltonian H_{cont}. Different colors represent the ≈750 lowest bulk eigenstates of 30 different patches of diameter 9 λ that contain around 250 local minima each. Between $V_0 \approx 1$–$10\,E_{\text{rec}}$, a clear energy gap separates the lowest bulk band from higher states. To minimize finite-size effects, boundary conditions are set similarly to Fig. 13(b). The inset shows the width of the gap for 30 different patches.

where $S_{ij} \equiv \langle w_i^{\text{NO}} | w_j^{\text{NO}} \rangle$ is the overlap matrix between NOWFs. The Löwdin transformation ensures a minimal distance between the orthogonalized and nonorthogonal sets [40], i.e.,

$$\sum_i \langle w_i - w_i^{\text{NO}} | w_i - w_i^{\text{NO}} \rangle = \min. \tag{4}$$

Therefore, applying a Löwdin transform onto the nonorthogonal maximally localized basis provides us with a maximally localized orthogonal and real-valued basis set. We note that the Löwdin transform fails in case of overcompleteness of the nonorthogonal basis, where the overlap matrix does not have maximal rank and therefore cannot be inverted. The success of the Löwdin transform is therefore a good check for overcompleteness of the initial nonorthogonal basis set.

In practice, the single-particle eigenstates $|E_k\rangle$ are extracted from a finite-difference formulation of the continuum Schrödinger equation using Lanczos' algorithm [41] (see Appendix A for details). The presented method for constructing WFs becomes exact in the limit of $R \to \infty$ and vanishing step size for the discretization, but fine grids limit the calculation in practice to relatively modest cutoff radii (typically on the order of 10 lattice sites, i.e., including around 250 to 300 neighboring lattice sites in the 2D case). The resulting approximate WFs converge towards the exact WFs when the cutoff radius R becomes much larger than the characteristic size of the WF and we found empirically that implementing the boundary conditions as a hard wall of finite height (cf. Fig. 13 in Appendix B) significantly speeds up the convergence (see Appendix C). We note that the NOWFs on all lattice sites are generated independently of each other; this step can therefore trivially be parallelized.

II. TWO-DIMENSIONAL EIGHTFOLD OPTICAL QUASICRYSTAL

We now apply the above method to the two-dimensional eightfold quasicrystal (8QC) shown in Fig. 2, which has recently been realized using ultracold atoms [28,29]. This continuum quasiperiodic lattice is closely related to the discrete eightfold Ammaan-Beenker lattice [42,43]. It is formed by superimposing two square optical lattices that are rotated by 45° with respect to each other and its optical potential (Fig. 2) is given by

$$V(\mathbf{r}) = V_0 \sum_{i=x,y,+,-} \sin^2(\mathbf{k}_i \cdot \mathbf{r} + \phi_i);$$
$$\mathbf{k}_i \in \frac{2\pi}{\lambda}\left\{\begin{pmatrix}1\\0\end{pmatrix}, \begin{pmatrix}0\\1\end{pmatrix}, \frac{1}{\sqrt{2}}\begin{pmatrix}1\\1\end{pmatrix}, \frac{1}{\sqrt{2}}\begin{pmatrix}1\\-1\end{pmatrix}\right\}. \tag{5}$$

Here, V_0 denotes the lattice depths and the $\mathbf{k}_i$ and ϕ_i are the wave vectors and offset phases of the individual lattices created by superimposing laser beams of wavelength λ. This potential is clearly long-range ordered, as it is fully deterministic and contains no randomness. At the same time, it cannot be periodic, as eightfold rotational symmetries are forbidden in periodic lattices [28]. The relative phases ϕ_i account for the phasonic degrees of freedom, which are relevant in the context of topological pumping [44]. However, for large static lattices, the phases become irrelevant for bulk properties of the 8QC, see Sec. III.

For the remainder of the paper, we will express all energies and lattice depths in units of the *recoil energy* $E_{\text{rec}} = \frac{\hbar^2 k^2}{2m}$, and all distances in terms of λ. For the calculation of U, we assume a $20\,E_{\text{rec}}$ deep retroreflected lattice generated using the same wavelength λ along the transverse direction. While we focus on the Bose-Hubbard model, we note that other types of Hubbard models (e.g., including longer-range interactions, or describing fermions with spin) can be similarly derived.

A. Extracting Wannier functions

The generation of WFs for the 8QC presents several challenges. In contrast to, e.g., the Aubry-André model [10], the present model cannot be expressed as a perturbation of a periodic model. Therefore, it is *a priori* not clear whether the lowest part of its single-particle energy spectrum can be described in terms of a single isolated band. Moreover, even

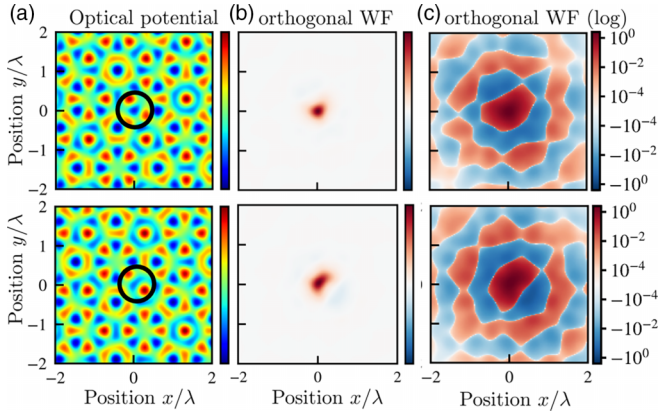

FIG. 4. (a) 8QC potential highlighting two different local minima for $V_0 = 2.5\,E_{\mathrm{rec}}$. (b), (c) Corresponding orthogonalized Wannier functions plotted on linear and logarithmic scales. As in periodic systems, WFs exhibit oscillating side lobes with exponential decaying amplitudes that are clearly visible when plotted on a logarithm scale.

provided such a lowest band exists, it is *a priori* not clear whether it would correspond to one Wannier function per local minimum.

To investigate whether an isolated lowest band exists, we compute the noninteracting energy spectrum of the bulk of the 8QC by direct numerical diagonalization of the continuum Hamiltonian (see Fig. 3). To obtain the bulk energy spectrum, we exclude eigenstates localized on the outer edge of the simulated finite-size patches. We find that for lattice depths $V_0 \approx 1$–$10\,E_{\mathrm{rec}}$, the lowest part of the bulk spectrum indeed forms an isolated band that is separated from the rest of the spectrum by a robust gap, independent of the chosen patch. Strikingly, we find that the lowest-energy subspace always contains essentially as many states as there are local minima in the finite patch (up to well-understood exceptions, treated in Appendix G). This implies that, for V_0 between 1 to $10\,E_{\mathrm{rec}}$, we can construct a Wannier basis for the lowest band by using one localized Wannier function per local minimum of the potential, analogous to conventional periodic lattices. We note that the 8QC contains less sites per area than a corresponding 2D square lattice, the ratio is equal to the inverse of the silver mean $\frac{2}{1+\sqrt{2}} \approx 0.8284$ (see Appendix F for details). We construct the corresponding NOWFs by following the method presented in Sec. I starting from the eigenstates in the lowest band. In order to facilitate the convergence of the NOWF already for small cutoff radii R, we apply specifically tailored boundary conditions that follow the shape of the outermost minima; see Appendix B for detailed discussion and Appendix C for numerical convergence checks. Afterwards, we apply a Löwdin transform on the NOWFs to obtain an orthogonal set of maximally localized WFs [Eq. (3)]. Examples of the resulting Wannier functions are shown in Fig. 4 and, similarly to periodic lattices, exhibit exponentially decaying oscillating side lobes that ensure orthogonality.

B. Bose-Hubbard model

We next obtain the 8QC Bose-Hubbard Hamiltonian by explicitly computing its matrix elements in the basis of WFs (see Fig. 5). We assume a scattering length of $a = 100\,a_0$,

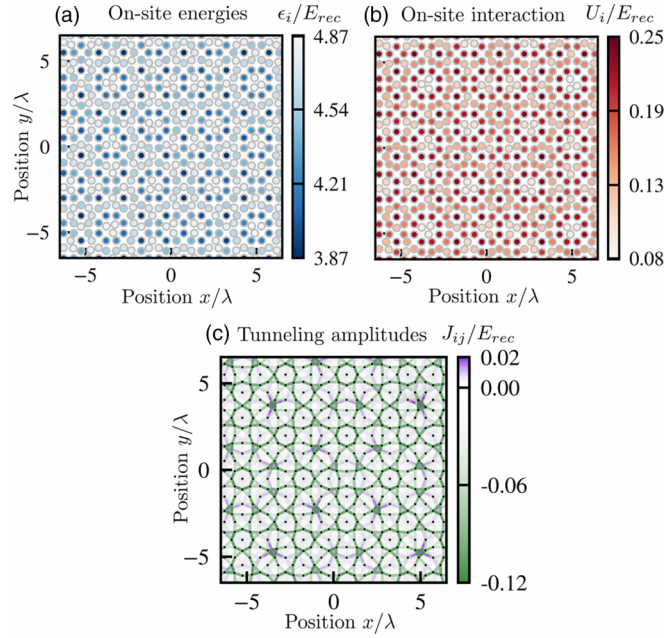

FIG. 5. Hubbard parameters for the 8QC for $V_0 = 2.5\,E_{\mathrm{rec}}$ corresponding to the potential shown in Fig. 2. Tunneling amplitudes J_{ij} (both negative and positive) are shown up to second-order neighbors. Onsite interactions assume a scattering length of $a = 100\,a_0$ and a $20\,E_{\mathrm{rec}}$ transverse lattice.

where a_0 denotes the Bohr radius, and a transverse lattice of depth $20\,E_{\mathrm{rec}}$. We observe that contrary to simpler models such as Aubry-André models, it is quasiperiodic in all three parameters. Furthermore, onsite energies ϵ_i and interaction energies U_i are anticorrelated: sites with high ϵ_i correspond to shallow minima and hence also have a low U_i, and vice versa; the same tendency was also noticed in optical lattices with weak quasiperiodic modulation [45]. While the most significant tunneling amplitudes have negative sign, the Hamiltonian also exhibits some small but non-negligible longer-range tunneling amplitudes with positive sign. Finally, we show in Appendix E that off-site interactions between neighboring sites can be safely neglected.

(a) Noninteracting energy spectrum. As an initial benchmark of the resulting Bose-Hubbard (BH) model, we use exact diagonalization in the noninteracting ($a = 0\,a_0$) case to compute the energy spectrum and eigenstates of a finite-sized lattice containing around 2800 sites, i.e., 10 times more than in the continuum calculation in Fig. 3. The resulting spectra (Fig. 6) contain a series of minigaps at intermediate lattice depths typical for quasiperiodic models.

The noninteracting physics of the 8QC is governed by the interplay between the tunneling elements J_{ij} and the energy differences (detunings) $\Delta_{ij} = \epsilon_i - \epsilon_j$ between lattice sites. Resonances, i.e., high ratios J_{ij}/Δ_{ij} between sites, favor hybridization of the corresponding Wannier functions and will lead to delocalization of the eigenstates. While all eigenstates are extended for weak lattices, increasing lattice depths V_0 leads to decreasing tunneling amplitudes and increasing detunings (cf. Fig. 7). Combined, these two mechanisms strongly decrease the number of resonances and eventually localize all eigenstates.

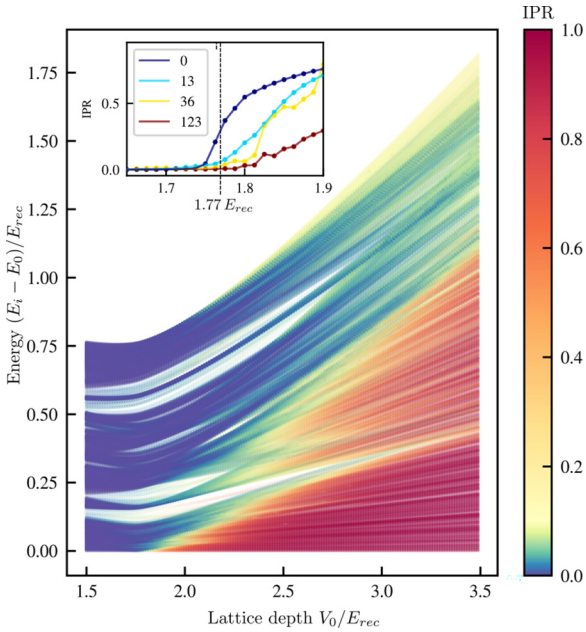

FIG. 6. 8QC: Noninteracting energy spectrum of the BH Hamiltonian. Color encodes the IPR of the eigenstates. Inset: IPR of the lowest (0) and the 13th, 36th, and 136th eigenstates, highlighting the localization transition.

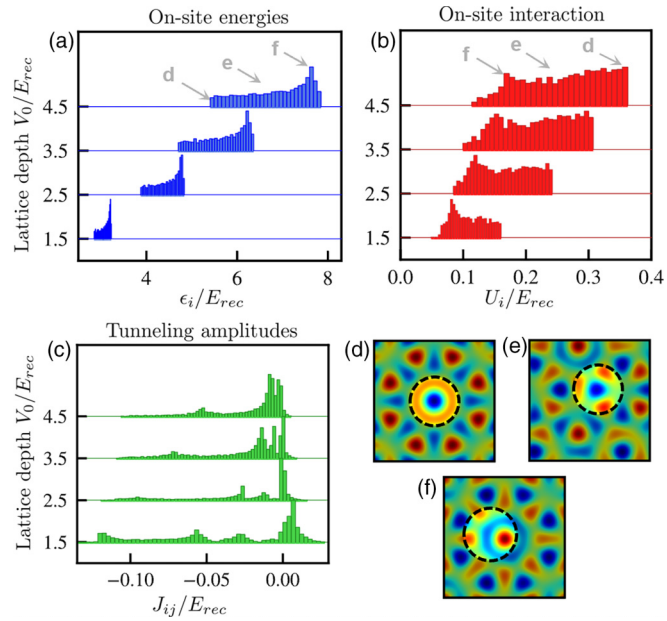

FIG. 7. (a)–(c) Histograms of 8QC Hubbard parameters (≈1600 sites) for various lattice depths V_0. Tunneling amplitudes are included up to second-order neighbors (see Appendix H for definition), and for $|J_{ij}| > 10^{-3}\,E_{\rm rec}$. Onsite interactions computed for a scattering length $a = 100\,a_0$ and a $20\,E_{\rm rec}$ transverse lattice. (d)–(f) Examples of lattice sites possessing different onsite and interaction energies.

To quantify the localization properties of the noninteracting eigenstates $|E_i\rangle = \sum_k c_k^i\,|w_k\rangle$, we compute their inverse participation ratio (IPR):

$$\mathrm{IPR}_i = \sum_k \left|c_k^i\right|^4. \tag{6}$$

An IPR of 1 means that the state is localized on a single lattice site, while the IPR of a fully delocalized state vanishes in an infinitely large system. The color code in Fig. 6 represents the IPR of all energy eigenstates as a function of the lattice depth V_0. The inset focuses on the IPR of some of the lowest-lying states. It shows that the ground-state undergoes a localization transition at a critical lattice depth in excellent agreement with the value $V_c = 1.77\,E_{\rm rec}$ reported in [29,46,47]. Moreover, Fig. 6 demonstrates that the excited states exhibit a mobility edge separating localized and delocalized states. This is consistent with what is seen in generalized Aubry-André models [13,14,27].

(b) Hubbard parameters. While numerical simulations based on the interacting BH Hamiltonian will be left to future work, we can already gain physical insight by inspecting the distributions of onsite energies $p(\epsilon)$, interactions $p(U)$, and tunneling amplitudes $p(J_{ij})$ (see Fig. 7). The shape of these distributions is very different from what is observed in truly disordered lattice, such as lattices with speckle potentials [48].

For instance, the distribution of onsite energies contains a sharp maximum reminiscent of a Van Hove singularity [Fig. 7(a)] and increasing the lattice depth V_0 causes the width of $p(\epsilon)$ to increase in an almost linear fashion [Fig. 8(a)]. In addition, the onsite energies form a continuous distribution without any sizable gaps.

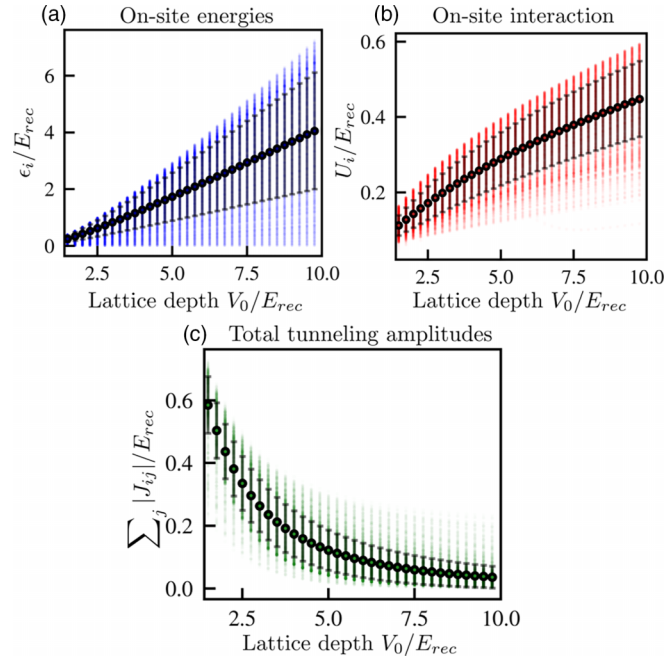

FIG. 8. (a)–(c) Distribution of 8QC Hubbard parameters (≈1600 sites) as a function of lattice depth V_0. Black dots and bars denote mean values and standard deviations of the distribution. Onsite energies are plotted relative to the lowest onsite energy. Onsite interactions computed for a scattering length $a = 100\,a_0$ and a $20\,E_{\rm rec}$ transverse lattice.

Increasing lattice depths also leads to increasing interaction strengths, with their mean scaling approximately as $\overline{U} \propto \sqrt{V_0}$ [see Figs. 7(b) and 8(b)], as expected from the decreasing width of the Wannier functions. The upper limit of $p(U)$ closely resembles the value of U expected for a 2D square lattice of depth $2V_0$. Indeed, the lattice sites sitting at the top of $p(U)$ distribution [Fig. 7(d)] are locally similar to the well of a square lattice of depth $2V_0$: both are surrounded by potential barriers of heights close to $4V_0$. In addition, Fig. 7 illustrates that irrespective of the lattice depth, the sites located in the deepest potential wells [Fig. 7(d)] are characterized by the lowest onsite energies and highest onsite interaction. Conversely, the highest onsite energies and lowest interaction occur in the shallowest potential wells [Fig. 7(f)].

Finally, the average tunneling amplitude [Figs. 7(c) and 8(c)] decreases broadly exponentially with increasing lattice depth, which is expected from the increasing potential barriers separating lattice sites and the narrower Wannier functions. We also note that a significant share of weak tunneling amplitudes is positive, which we attribute to tunneling between higher-order neighbors (see Appendix H for details).

III. CONFIGURATION SPACE: DESCRIBING THE QUASICRYSTAL IN THE INFINITE-SIZE LIMIT

There are two main motivations to try to find an alternative description of the quasicrystalline lattice: the absence of periodicity means that there is no simple reciprocal space description, and it would be ideal to have a suitable replacement, i.e., an aperiodic analog of the Brillouin zone suitable for studying thermodynamic or topological properties of the system. In addition, the sites of the 8QC all differ in shape and local surrounding and any finite patch will only contain a subset of all possible sites. *A priori*, one can therefore never be sure whether increasing the simulated system size might introduce additional rare types of lattice sites, changing the results of the simulation.

To overcome this limitation and arrive at a powerful, compact representation, we sort the lattice sites based on their shapes and local environments and arrive at a bounded configuration space that enables us to describe the infinite quasicrystal. This procedure is similar to configuration-space descriptions of stacked bilayer systems [30–32] and we demonstrate in Appendix I that it directly corresponds to the perpendicular space of discrete octagonal quasicrystals [33–37].

We start by recalling that the 8QC is formed by superimposing two square lattices rotated by 45° (Fig. 2), which is reminiscent of a stacked bilayer system. We refer to the lattice oriented along the x and y axes as the XY lattice. The other square lattice is referred to as the diagonal (D) lattice. Figure 9 shows a finite patch of the 8QC potential, where the minima of the XY and D lattices are indicated by red and blue dots. Deep wells in the quasicrystal correspond to closely spaced minima in the XY and D lattices. Conversely, more separated minima of the XY and D lattices result in a shallower minimum in the quasicrystal. Therefore, our mapping procedure characterizes each 8QC lattice site in terms of the local displacement $\mathbf{\Phi}$ between the XY and D square lattices.

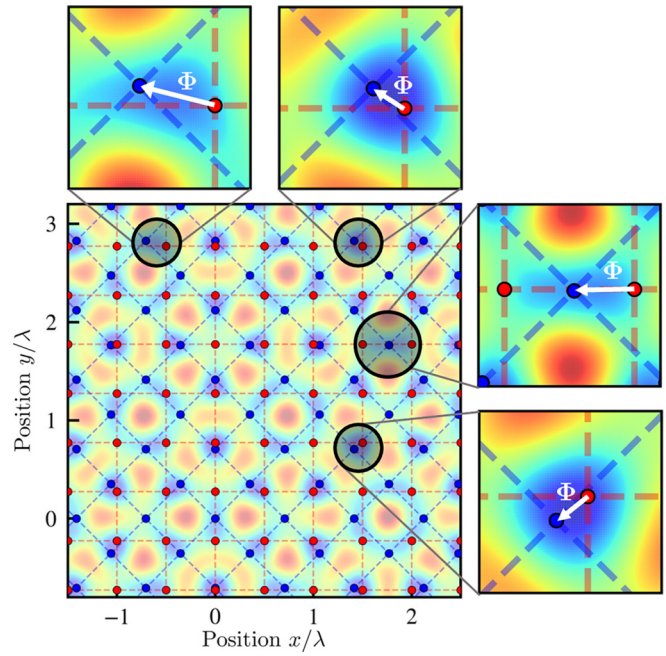

FIG. 9. The 8QC potential (background) is formed by superimposing two square lattices (red and blue grids). Insets: For every minimum $\mathbf{r_i}$ of the 8QC, the vector $\mathbf{\Phi}(\mathbf{r_i})$ denotes the displacement between the closest minima of the two square lattices and thereby uniquely defines the local potential. Deep sites correspond to small local displacements $\mathbf{\Phi}$, while large $\mathbf{\Phi}$ indicate shallow sites.

For every minimum in the potential $\mathbf{r_i} = (x_i, y_i)$, we compute its coordinates $\mathbf{\Phi}_{\mathrm{XY}}(\mathbf{r_i})$ and $\mathbf{\Phi}_{\mathrm{D}}(\mathbf{r_i})$ within the unit cells of both the XY and D lattices:

$$\mathbf{\Phi}_{\mathrm{XY}}(\mathbf{r}) = \left[\left(x + \frac{\phi_1}{k}\right) \bmod d\right] \mathbf{e}_x + \left[\left(y + \frac{\phi_2}{k}\right) \bmod d\right] \mathbf{e}_y, \tag{7}$$

$$\mathbf{\Phi}_{\mathrm{D}}(\mathbf{r}) = \left[\left(\frac{x+y}{\sqrt{2}} + \frac{\phi_3}{k}\right) \bmod d\right] \mathbf{e}_+ + \left[\left(\frac{x-y}{\sqrt{2}} + \frac{\phi_4}{k}\right) \bmod d\right] \mathbf{e}_-. \tag{8}$$

Here, $d = \lambda/2$ denotes the lattice constant of the square lattices, $\mathbf{e}_x$, $\mathbf{e}_y$ are the unit vectors along the x and y directions, $\mathbf{e}_\pm = \frac{\mathbf{e}_x \pm \mathbf{e}_y}{\sqrt{2}}$, and the ϕ_i are the four phases introduced in Eq. (5). For every site $\mathbf{r_i}$, the vector $\mathbf{\Phi}(\mathbf{r_i}) \equiv \mathbf{\Phi}_{\mathrm{XY}}(\mathbf{r_i}) - \mathbf{\Phi}_{\mathrm{D}}(\mathbf{r_i})$ then encodes the local displacement between the XY and D lattices and thereby fully describes the shape of the minimum and its local surroundings. As shown in Fig. 10, the vectors $\mathbf{\Phi}(\mathbf{r_i})$ describing the sites of the 8QC form an octagon of inscribed radius $d/2$, where the size stems from the periodicity of the two square lattices.

This configuration-space representation has the following properties: (1) In the infinite-size limit, the octagon is densely and uniformly populated with lattice sites (see Appendix H) and can therefore be used to derive statistical estimates about the lattice. We notice that this is identical to the perpendicular spaces of octagonal discrete quasiperiodic lattices [37,49]. (2)

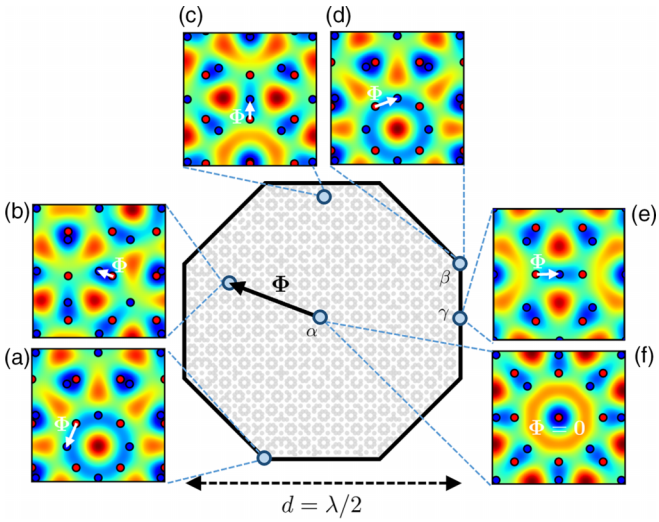

FIG. 10. In the infinite-size limit, the configuration-space positions $\mathbf{\Phi}$ of the 8QC lattice sites densely and uniformly populate an octagon, whose periodic boundaries are given by the mod operations in Eq. (7). (a)–(f) Show the 8QC potential for various positions on the octagon. Dots in the octagon denote the configuration-space positions of 2800 lattice sites.

Due to the aperiodicity of the lattice, every point $\mathbf{\Phi}$ within the octagon corresponds to one unique lattice site. (3) Analogous to the Brillouin zone in periodic crystals, the mod d operation implies periodic boundary conditions for this configuration space, i.e., every edge of the octagon can be identified with the opposing edge. These periodic boundary conditions imply that the octagon possesses the topology of a two-hole torus: it is an orientable surface with genus 2 [50]. In particular, the eight corners of the octagon are one unique point. (4) Symmetry points or lines of the octagon directly correspond to symmetry points or lines of the quasicrystal. For example, the center and corners of the octagon correspond to the two possible global eightfold rotational symmetry centers of the lattice [Figs. 10(f) and 10(a)]. By construction, these two can never be found together in the same realization of the 8QC, and most choices of ϕ_i will lead to none of them.

This configuration-space construction allows one to draw several conclusions regarding the infinite-size 8QC and will enable novel studies on topology in quasicrystals, as it provides a compact manifold on which, e.g., Berry curvature and related quantities can be defined. The concept of configuration space generalizes directly to other quasiperiodic lattices. For example, the configuration space of the one- and two-dimensional Aubry-André models can be constructed as a circle and a torus [51], respectively). While we cannot provide a general criterion, we expect that such constructions can be applied generically to quasiperiodic models that can be constructed via a cut-and-project procedure.

A. Hubbard model in configuration space

We can now reexpress the BH Hamiltonian of the 8QC entirely in the compact and densely populated configuration space. This is achieved by mapping the real-space coordinates

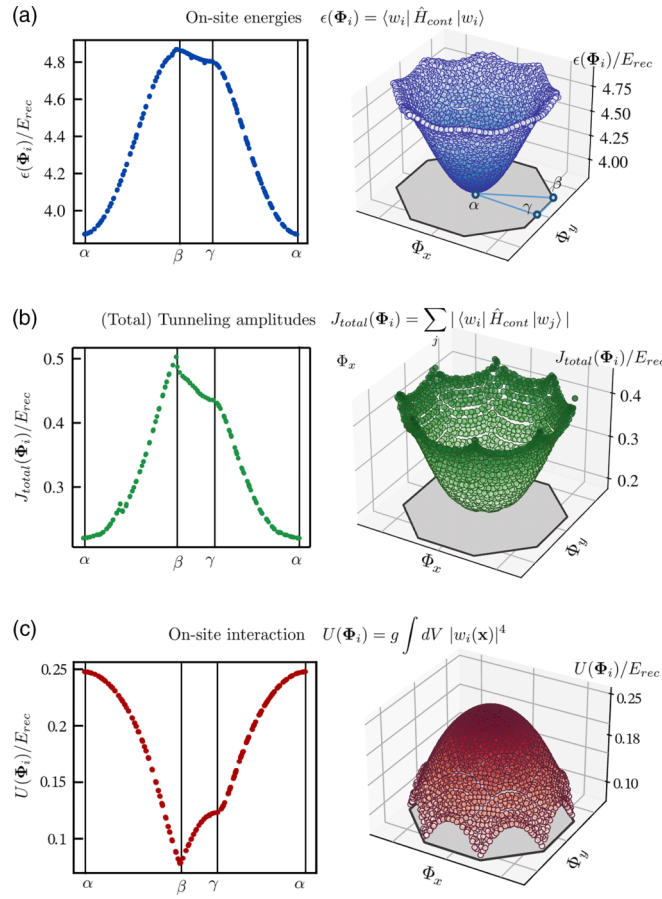

FIG. 11. 8QC: The Hubbard Hamiltonian can be reexpressed in configuration space, i.e., in the space of local displacements $\mathbf{\Phi}$. In this representation, the Hubbard parameters form smooth and eightfold-symmetric surfaces $\epsilon(\mathbf{\Phi})$, $U(\mathbf{\Phi})$, and $J(\mathbf{\Phi}, \mathbf{\Phi}')$. The α, β, and γ points are shown in (a). Figures show 2800 sites. Onsite interactions are computed for a scattering length $a = 100\, a_0$ and $20\, E_{\text{rec}}$ transverse lattice. For clarity, (b) shows the total tunneling amplitude per site $J_{\text{total}}(\mathbf{\Phi_i}) = \sum_{i \neq j} |J_{ij}|$. The individual tunneling amplitudes $J(\mathbf{\Phi}, \mathbf{\Phi}')$ in configuration space are discussed in Appendix H.

$\mathbf{r}_i$ of all sites of the 8QC to the corresponding $\mathbf{\Phi}(\mathbf{r}_i)$:

$$H_{\text{BH}} = \sum_{\mathbf{\Phi}} \epsilon(\mathbf{\Phi}) \hat{a}^\dagger_{\mathbf{\Phi}} \hat{a}_{\mathbf{\Phi}} + \sum_{\mathbf{\Phi} \neq \mathbf{\Phi}'} J(\mathbf{\Phi}, \mathbf{\Phi}') \hat{a}^\dagger_{\mathbf{\Phi}} \hat{a}_{\mathbf{\Phi}'} + \sum_{\mathbf{\Phi}} \frac{U(\mathbf{\Phi})}{2} \hat{n}_{\mathbf{\Phi}} (\hat{n}_{\mathbf{\Phi}} - 1). \tag{9}$$

Here, $\hat{a}_{\mathbf{\Phi}}$ is the annihilation operator for the WF at the site with coordinate $\mathbf{\Phi}$ in configuration space. This expression emphasizes that in configuration space, which is a compact and uniformly dense space with periodic boundaries, the 8QC is entirely described by the functions $\epsilon(\mathbf{\Phi})$, $J(\mathbf{\Phi}, \mathbf{\Phi}')$, $U(\mathbf{\Phi})$. These are shown in Fig. 11 and reveal a striking property: contrary to the fractal structure in real space, the Hubbard parameters form smooth functions in configuration space. This directly follows from the construction of configuration space, where an infinitesimal move in $\mathbf{\Phi}$ implies an infinitesimal relative displacement between the XY and D square lattices and hence a smooth change of the resulting potential. In turn, the

Wannier function hosted on the corresponding lattice site will also undergo an infinitesimal change, resulting in the observed smooth changes of all local properties. As a consequence, onsite energy, interaction, tunneling amplitudes, or any other local property must be smooth in configuration space.

Two important consequences follow from the smoothness of Hubbard parameters in configuration space. First, arbitrary large Hubbard Hamiltonians can now be obtained at negligible computational cost, for example, by computing Wannier functions for a finite number of points in configuration space and interpolating between them, or by direct interpolation of the Hubbard parameters. Second, the physics of the quasicrystal is, for sufficiently large system sizes, unaffected by the specific values of the phases ϕ_i. While they amount to global translations in configuration space, the dense sampling ensures that Eq. (9) remains effectively unaffected.

Turning to the shape of these surfaces, we observe that the sites close to the center of the octagon [Fig. 10(f)] correspond to almost perfectly overlapping minima of both square latices and are hence located within the deepest potential wells in real space. Therefore, they possess low onsite energy $\epsilon(\mathbf{\Phi})$, high onsite interaction energy $U(\mathbf{\Phi})$, and low total tunneling amplitudes $J_{\text{total}}(\mathbf{\Phi_i}) = \sum_{i\neq j} |J_{ij}|$. Conversely, sites corresponding to the corners of the octagon [Figs. 10(a) and 10(f)] are located on shallow and high-lying potential wells. They possess the highest onsite energies, the lowest onsite interaction, and highest tunneling amplitudes.

As a side note, we notice that the onsite energies [Fig. 11(a)] can be approximated by a simple analytical expression:

$$\epsilon(\mathbf{\Phi}) \approx \Delta_0 + \Delta \sum_{i=1}^{4} \sin^2\left(\frac{\mathbf{k}_i}{|\mathbf{k}_i|} \cdot \mathbf{\Phi}\right) \tag{10}$$

for V_0 between 1.5 to $10\,E_{\text{rec}}$. This approximation, whose form is surprisingly reminiscent of the lattice potential in Eq. (5), has an average relative root-mean-square error smaller than 1%. The individual tunneling amplitudes $J(\mathbf{\Phi}, \mathbf{\Phi}')$ are more intricate and are discussed in Appendix H, where we also show how the configuration space picture allows us to unambiguously define a hierarchy of first-, second-, and higher-order neighbors in a matter reminiscent of the fractal structure found in momentum space [28]. First-order neighbors and the lines connecting them form the well-known Ammaan-Beenker tiling. We emphasize, however, that there can be significant tunneling elements also connecting second-order neighbors. In contrast to the Ammaan-Beenker tiling, the 8QC is hence not bipartite. In future studies, it will be of interest to determine whether exact closed-form solutions can be obtained for the functions $\epsilon(\mathbf{\Phi})$, $U(\mathbf{\Phi})$, and $J(\mathbf{\Phi}, \mathbf{\Phi}')$.

B. Validity of single-band picture

The BH Hamiltonian presented in this work only considers the lowest band, i.e., one WF per lattice site. This is sufficient as long as temperature, chemical potential, and onsite interaction energies are smaller than the energy difference to the first excited WFs. The extension to more WFs per lattice site is left to future research, but we can extract the approximate onset of the second band already from the spectra of the continuum Hamiltonian for small systems (see Fig. 3). These are indicated by the black dashed line in Fig. 12, where the blue dots indicate the onsite energies $\epsilon(\mathbf{\Phi})$, and the red dots indicate the energy needed for a second particle on the same site, i.e., $\epsilon(\mathbf{\Phi}) + U(\mathbf{\Phi})$. We consider a transverse confining lattice of depth $V_z = 20\,E_{\text{rec}}$ and find that for lattice depths V_0 between 1 and $9\,E_{\text{rec}}$, we can reach a scattering length $a_{\text{max}} \approx 400\,a_0$ before doubly occupied sites begin to overlap with higher bands (Fig. 12). This indicates the validity of the single-band model in the relevant regimes.

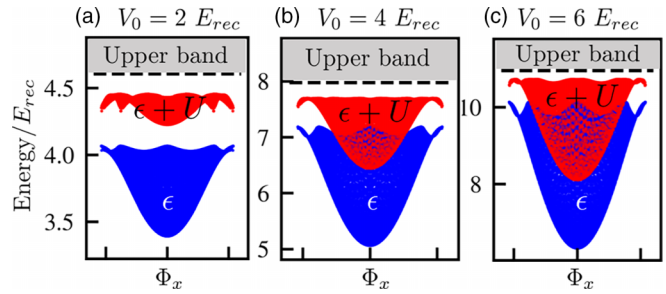

FIG. 12. 8QC: Estimation of maximal interaction energy achievable without exciting atoms into the higher bands using configuration space. The blue spectrum indicates the onsite energies $\epsilon(\mathbf{\Phi})$, while the red dots correspond to the energy needed for a second particle on the same site, i.e., $\epsilon(\mathbf{\Phi}) + U(\mathbf{\Phi})$. We consider $20\,E_{\text{rec}}$ transverse confining lattice and a scattering length $a = 400\,a_0$.

C. Mott-insulating phases

The precise ground-state phase diagram of the interacting 8QC will require large-scale numerical simulations (e.g., quantum Monte Carlo [52]) that will be facilitated by the Hubbard model developed in this work. One might, in analogy to other disordered or quasiperiodic lattices, expect it to contain superfluid and Mott-insulating phases that are separated by the compressible Bose-glass phase [45,47,53–63]. While the existence of Mott-insulating phases is *a priori* not clear, we can already draw some conclusions from the developed Hubbard model.

In the atomic limit, where tunneling can be neglected, and in the presence of a band gap above the lowest band, an incompressible Mott-insulating (MI) phase with one atom per site [i.e., $\frac{2}{1+\sqrt{2}} \approx 0.83$ atoms per $(\lambda/2)^2$, see Appendix F] will exist whenever

$$\epsilon(\mathbf{\Phi}) + U(\mathbf{\Phi}) > \max_{\mathbf{\Phi}'}[\epsilon(\mathbf{\Phi}')] \quad \forall\ \mathbf{\Phi}, \tag{11}$$

i.e., whenever the interaction dominates over the spread in onsite energies (see Fig. 12). This suggests that for relatively large lattice depths (but with $V_0 < 10\,E_{\text{rec}}$ such that a finite band gap exists) and sufficiently high scattering lengths, there will always be an incompressible MI phase with unit filling. We note, however, that excitations of this Mott insulator or its extension to finite temperatures would likely not be accurately described by the current BH model, as double occupancies could hybridize with the excited band.

Furthermore, Fig. 8 highlights that with increasing lattice depth, the spread in $\epsilon(\mathbf{\Phi})$ grows faster than the average onsite interaction. Equation (11) therefore implies that the transition

from Bose glass to MI will for deeper lattices shift to larger scattering lengths. This is in stark contrast to a periodic lattice, where the transition from superfluid to MI shifts to smaller scattering lengths for deeper lattices.

As a third important conclusion, the continuous distribution of onsite energies $\epsilon(\mathbf{\Phi})$ in the thermodynamic limit directly implies that, at least in the atomic limit, there are no incommensurate Mott phases below unit filling, as such states would always be gapless and compressible. This suggests that the MI states with fractional fillings found in recent quantum Monte Carlo simulations of the continuum model [47] might be limited to finite system sizes, where configuration space by necessity is only sampled coarsely.

IV. CONCLUSION

We presented a general numerical method for computing the Wannier functions and Hubbard Hamiltonians of nonperiodic potentials. This method was then applied to construct the Bose-Hubbard Hamiltonian of the two-dimensional eightfold-symmetric optical quasicrystal (8QC). As a benchmark, we reproduced the localization transition in the noninteracting ground state and obtained excellent agreement with earlier results [29,46,47].

In a second part, we introduced a configuration-space representation of the 8QC. This representation, inspired by existing schemes for incommensurate bilayer systems, is an aperiodic analog of the Brillouin zone, and as such enables the description of the quasicrystal in the infinite-size limit by ordering the lattice sites in terms of their shape and local surroundings. We showed that the Hubbard model of an infinite 8QC can be reexpressed on a dense and compact octagonal configuration space with periodic boundary conditions. In this representation, the Hubbard parameters take the form of smooth functions.

This Hubbard model opens the door to large-scale numerical simulations of quasicrystalline optical lattices, and the developed configuration space enables new analytic arguments about the many-body physics and topological structure of these models.

In future studies, it will be of interest to apply the configuration-space picture to other quasiperiodic lattices, such as Aubry-André models and models interpolating between quasicrystalline and Aubry-André limits.

All the data regarding the Hubbard Hamiltonian of the 8QC and the associated Wannier functions are available for public access [64].

ACKNOWLEDGMENTS

This work was partly funded by the European Commission ERC Starting Grant QUASICRYSTAL, the EPSRC Grant No. EP/R044627/1, and Programme Grant DesOEQ (Grant No. EP/P009565/1). For the purpose of open access, the author has applied a Creative Commons Attribution (CC BY) licence to any Author Accepted Manuscript version arising. We are very thankful to S. Bhave, G. Nixon, L, Reeve, B. Song, and J.-C. Yu from the Quasicrystal Team, along with C. Duncan, A. Daley, A. Ashoka, J. Crabbe, and A. Safari for helpful discussions.

APPENDIX A: FINITE-DIFFERENCE SCHRÖDINGER EQUATION

We use the finite-difference Schrödinger equation (FDS) for the numerical solution of the Schrödinger eigenvalue equation $\hat{H}\,|\psi_i\rangle = E_i\,|\psi_i\rangle$, illustrated below in the one-dimensional case for simplicity. Deriving the FDS Hamiltonian consists of writing the matrix elements of the Hamiltonian $\hat{H} = -\frac{1}{4\pi^2}\Delta + V(x)$ (written in units of E_{rec}) in a discretized position basis $|x_i\rangle$ with grid spacing $\delta x = \frac{L}{N}$, where L is the system size and N the number of grid points.

Using a finite-difference approximation, we can write the Laplacian as

$$\Delta\psi(x) \approx \frac{\psi(x+\delta x) - 2\psi(x) + \psi(x-\delta x)}{(\delta x)^2}.$$

Therefore, its matrix elements in the discretized basis are

$$\langle x_i|\,\Delta\,|x_j\rangle = \frac{\delta_{i+1,j} - 2\delta_{i,j} + \delta_{i-1,j}}{(\delta x)^2}.$$

The potential operator $\hat{V}$ is diagonal in the discretized basis and its matrix elements are $\langle x_i|\,\hat{V}\,|x_j\rangle = V(x_i)\;\delta_{i,j}$. Consequently, we can write the matrix elements of the FDS Hamiltonian as

$$\langle x_i|\,H\,|x_j\rangle = -\frac{1}{4\pi^2}\,\langle x_i|\,\Delta\,|x_j\rangle + \langle x_i|\,\hat{V}\,|x_j\rangle \tag{A1}$$

$$= -\frac{1}{4\pi^2}\,\frac{\delta_{i+1,j} - 2\delta_{i,j} + \delta_{i-1,j}}{(\delta x)^2} + V(x_i)\,\delta_{i,j}. \tag{A2}$$

We use a numerical matrix eigenvalue solver based on Lanczos' algorithm [41] to obtain the lowest eigenvalues E_i and corresponding eigenvectors $|E_i\rangle = \sum c_j^i\,|x_j\rangle$ of the finite-difference Hamiltonian H with open boundary conditions.

The FDS algorithm is naturally limited by Nyquist's theorem. In order for the algorithm to be accurate, the inverse of the discretization step should always be at least twice the maximal momentum contained in the Fourier transform of the considered state. Consequently, for a given discretization step size, the precision of the obtained solution decreases for higher-lying states.

APPENDIX B: BOUNDARY CONDITIONS FOR GENERATING THE WANNIER FUNCTIONS

The boundary conditions for calculating the NOWFs consist of a hard wall of height $4\,V_0$, whose shape is generated in two steps. We first compute the convex hull of the set of all lattice sites within the cutoff radius R, and then enlarge it by $0.17\,\lambda$ (blue line on Fig. 13). This results in a boundary that still strongly affects the wave function on the wells closest to the cutoff radius. Therefore, we calculate a second boundary that closely matches the shapes of the wells (red line on Fig. 13). This is created from the contour line sitting 15% of the total amplitude of the optical potential (which is $4V_0$) above the bottom of the potential wells, and enlarged by a factor of 2.5. Joining these two then leads to the boundary condition shown in Fig. 13(b) that improves convergence for small cutoff radii.

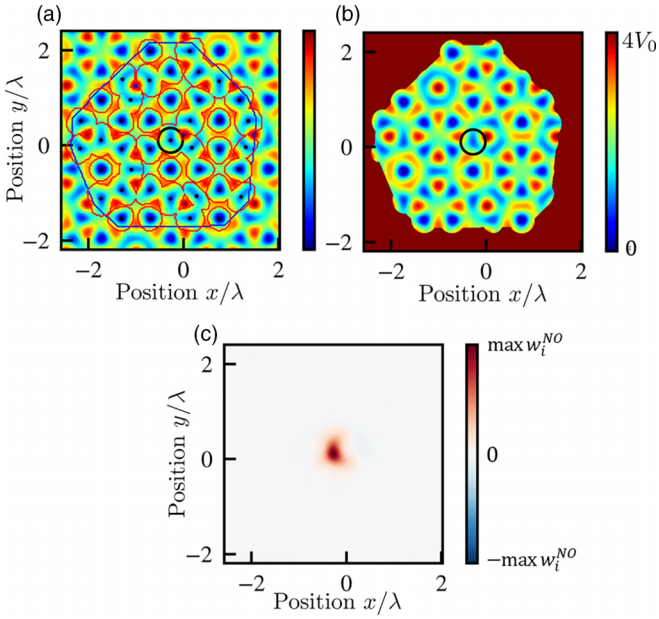

FIG. 13. (a) The boundary conditions for generating the NOWF (b) are generated by combining two criteria. One is the convex hull of the set of all sites within the cutoff radius enlarged by $0.17\,\lambda$ (blue line). The second combines individual boundaries around each lattice site (red), that consist of the contour lines sitting 15% above the bottom of the potential wells, enlarged by a factor of 2.5. The resulting boundary wall is shown in (b). Afterwards, a nonorthogonal Wannier function (c) is constructed by localizing a linear combination of eigenstates around the central minimum (dark circle).

APPENDIX C: CONVERGENCE CHECKS

The convergence of the BH parameters is controlled by two parameters: the grid spacing δx and the cutoff radius R for the generation of NOWFs.

Figure 14 shows the result of a convergence study in the grid spacing at a lattice depth of $9\,E_{\mathrm{rec}}$. We estimate the convergence by comparing the Hubbard parameters (onsite energies, interaction, and nearest-neighbor tunneling amplitudes) to a "converged" solution computed with the smallest

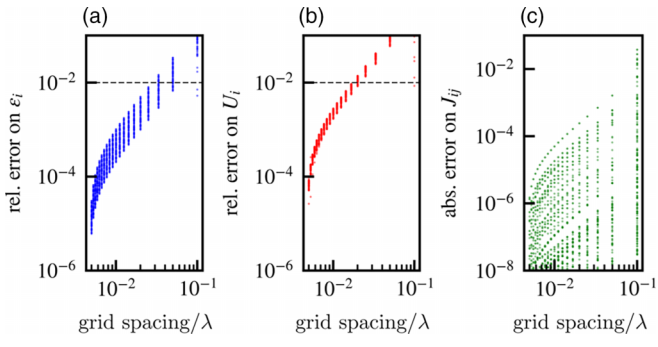

FIG. 14. Convergence of onsite energies (a), onsite interaction (b), and nearest-neighbor tunneling amplitudes up to second-order neighbors (c) as a function of the numerical grid spacing δx at $V_0 = 9\,E_{\mathrm{rec}}$. System containing 63 lattice sites. Errors are obtained by comparing the results with a "converged" solution computed for a grid spacing of $\delta x_{\mathrm{min}} = 4.76\times10^{-3}\,\lambda$.

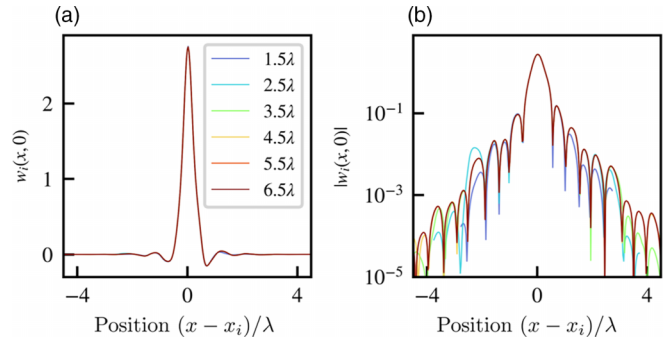

FIG. 15. Convergence of an 8QC Wannier function as a function of cutoff radius R on linear (a) and logarithmic (b) scales. Figure only shows the horizontal cross section of the 2D Wannier function. $V_0 = 1.5\,E_{\mathrm{rec}}$.

grid spacing of $\delta x_{\mathrm{min}} = 4.76\times10^{-3}\,\lambda$ on a system of 63 lattice sites. In the case of the tunneling elements, we considered the absolute error instead of the relative error, as very small tunneling amplitudes can have large relative errors without affecting the physics of the model. As a result, we set the grid spacing for all lattice depths to $\delta x = 0.03\,\lambda$, resulting in an accuracy of $\approx$1%. This requirement in grid spacing is most stringent at the highest lattice depth, as deeper lattices reduce the spread of the WFs.

Figure 15 illustrates the convergence of a Wannier function for increasing cutoff radii R, for a relatively shallow depth of $V_0 = 1.5\,E_{\mathrm{rec}}$. As seen on a logarithmic scale, the relevant side lobes (and thereby the tunneling elements) quickly converge when R is increased.

To assess the convergence of the WF more quantitatively, Fig. 16 shows the effect of varying the cutoff radius R on the convergence of onsite energies, interaction, and nearest-neighbor tunneling amplitudes of 66 lattice sites for $V_0 = 1.5\,E_{\mathrm{rec}}$. We estimate convergence by comparing them with the result of a "converged" solution computed with a cutoff radius of $7\,\lambda$. We expect the requirement in cutoff radius R to be more stringent at low lattice depth where the Wannier functions are more spread out. As a result, we set the cutoff radius to $R = 4\,\lambda$ for all lattice depths (except where stated otherwise in the text). As an additional test, we used the same δx and R to generate the Hubbard Hamiltonian of a finite-size square

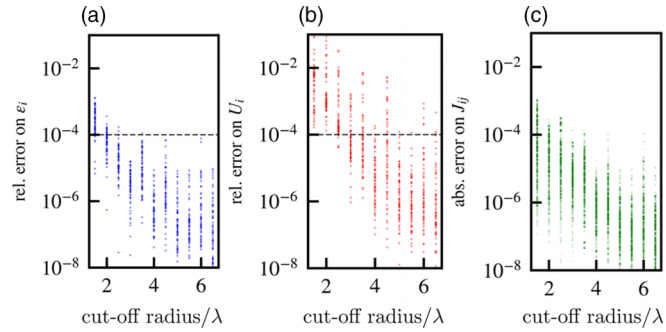

FIG. 16. Convergence of the onsite energies (a), onsite interaction (b), and tunneling amplitudes up to second-order neighbors (c) as a function of the cutoff radius R. $V_0 = 1.5\,E_{\mathrm{rec}}$. System containing 66 lattice sites. Errors are obtained by comparing the results with a "converged" solution computed for a cutoff radius of $7\,\lambda$.

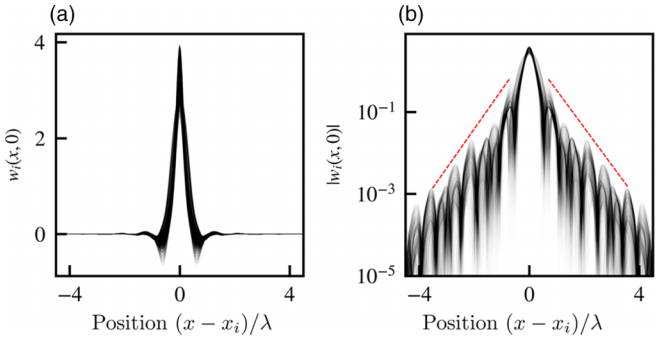

FIG. 17. Cross section of 1600 different Wannier functions on linear (a) and logarithmic (b) scales. $V_0 = 1.5\,E_{\mathrm{rec}}$. Red lines indicate the exponentially decaying side lobes.

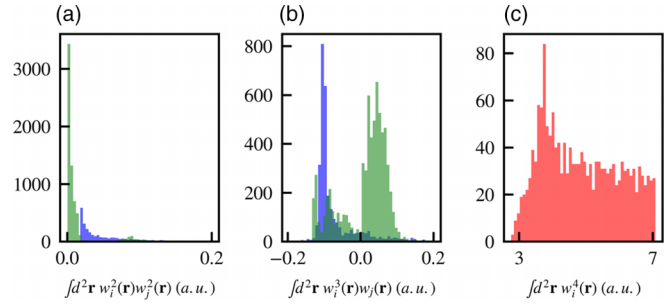

FIG. 18. (a), (b) Histograms of two-body amplitudes between neighboring sites. First-order neighbors in blue and second-order neighbors in green. (c) Corresponding histogram for two-body onsite interaction. Lattice depth is $V_0 = 1.5\,E_{\mathrm{rec}}$.

periodic lattice, and compared the nearest-neighbor tunneling amplitudes to the result expected from maximally localized Wannier functions computed using Bloch waves. In the range $V_0 = 2$ to $10\,E_{\mathrm{rec}}$, the relative error in onsite interaction and nearest-neighbor tunneling was always below 3×10^{-2}.

APPENDIX D: EXPONENTIAL LOCALIZATION OF THE WANNIER FUNCTIONS

Figure 17 shows cross sections of 1600 different 8QC Wannier functions, obtained for a low lattice depth of $V_0 = 1.5\,E_{\mathrm{rec}}$, i.e., below the ground-state localization transition. These exhibit exponentially decaying side lobes that are clearly visible as a linear decay in logarithmic scale (red lines).

APPENDIX E: OFF-SITE INTERACTIONS

Atoms on neighboring sites can in principle interact through various two-body processes due to the overlap of the corresponding Wannier functions [38,65,66]. The matrix elements of these processes involve integrals of the form

$$U_{ijkl} \propto \int d^2\mathbf{r}\, w_i^*(\mathbf{r}) w_j^*(\mathbf{r}) w_k(\mathbf{r}) w_l(\mathbf{r}), \tag{E1}$$

which considers Wannier functions located on different lattice sites. The most significant processes involve just one pair of sites (U_{iijj} and U_{iiij}). To check whether these off-site processes could be significant for the 8QC, we explicitly compute the overlap integrals for pairs of neighboring sites, in a shallow lattice ($V_0 = 1.5\,E_{\mathrm{rec}}$) containing around 1600 sites. As seen in Fig. 18, these off-site processes are always at least one order of magnitude smaller than the lowest onsite interaction energies. We can therefore safely neglect them for all lattice depths above $1.5\,E_{\mathrm{rec}}$, where the off-site processes are even further suppressed due to the increased confinement of the WFs.

APPENDIX F: DENSITY OF SITES OF THE EIGHTFOLD OPTICAL QUASICRYSTAL

The configuration-space picture can be employed to derive the exact density of lattice sites in the eight-fold optical quasicrystal: we first note that in the limit of vanishingly weak beams in the diagonal k_+ and k_- directions, the resulting potential contains as many sites as the usual square lattice, which has a density n_{square} of 1 site per $(\lambda/2)^2$. In addition, the configuration space of this lattice with weak diagonal beams now constitutes a densely populated square of side d. Increasing the weak diagonal beams to restore the eightfold symmetry adds new periodic boundary conditions along the diagonal directions in configuration space and reduces the square to the octagon shown in Fig. 10. Since the density in configuration space remains constant, we can directly infer that the ratio of the density of sites in the 8QC ($n_{8\mathrm{QC}}$) to the square lattice is given by the ratio of the area of the octagon to the square, i.e., the inverse of the silver mean:

$$\frac{n_{8\mathrm{QC}}}{n_{\mathrm{square}}} = \frac{2}{1+\sqrt{2}} \approx 0.8284. \tag{F1}$$

APPENDIX G: EXCEPTIONAL MINIMA AT THE BOUNDARY OF CONFIGURATION SPACE

As mentioned in Sec. II, the lowest band of the 8QC lattice contains one state per local minimum of the potential, up to some exceptional lattice sites. Indeed, some very shallow local minima exist that do not host a Wannier function in the lowest band [for an example see the red cross in Fig. 19(c)]. Careful inspections shows that in configuration space these minima are always located just outside the edge of the octagon and that they correspond to the higher minima of asymmetric double wells [see the inset on Fig. 19(c)]. The other minimum of the double well is then always located inside the octagon. Numerically diagonalizing a patch containing such a double well shows that only the lower state of this double well contributes to the ground band, while the higher state can be found in the excited band. The code accounts for the lowest band state hosted in the double well by generating one Wannier function localized around the minimum lying inside the octagon. By construction, this state will correspond to the lower eigenstate of the double well.

The minima sitting exactly on the boundaries of the octagon form perfectly symmetric double wells in real space [see Figs. 19(a) and 19(b)]. In this configuration, the symmetric combination belongs to the lowest band, while the antisymmetric combination is part of the excited band. Such configurations of lattice sites have also been observed in discrete octagonal quasicrystals obtained from cut-and-project procedures from hypercubic four-dimensional lattices [67].

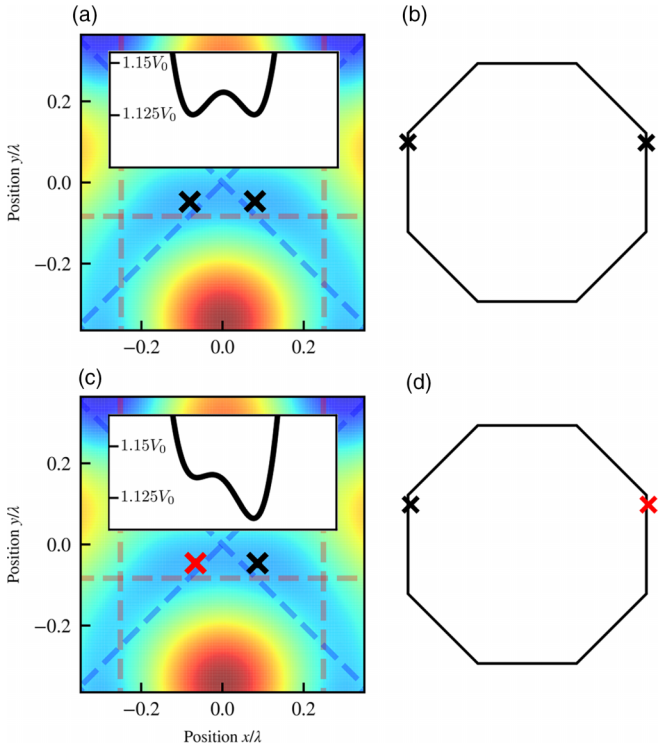

FIG. 19. Sites (crosses) located close to the edges of the octagon (right) correspond to very shallow double wells in real space (left), which contain only one state in the lowest band. (a), (b) Show the case of a perfectly symmetric double well, lying exactly on the edge of the octagon. Both minima (black crosses) are separated by a shallow barrier of height $\approx 0.01V_0$. (c), (d) Show an asymmetric double well, one of the minima (red cross) lies outside of the octagon. Insets show a 1D cross section of the double-well potentials.

As these constitute a set of measure zero in configuration space they are statistically irrelevant in the thermodynamic limit and hence require no special treatment.

Another specific case arises for the minima located exactly on the eight corners of the octagon. In this case, the potential forms a perfectly eightfold-symmetric ring containing eight local minima separated by very weak potential barriers (see Fig. 20). This configuration is a center of global rotational symmetry of the 8QC, and can hence occur only once.

We can obtain an estimate for the energies of the states hosted on this ring using exact diagonalization of a patch containing the ring. Figure 21 shows the energies of theses states as a function of lattice depth, and compares them to the typical energy spectrum of the rest of the lattice. As we see, the ring contains three low-energy states that are located at the upper limit of the lowest band. The five higher-lying states are instead located within the excited bands.

Using the classification of first-order neighbors developed below, we can see that in situations close to, but not equal to, the eightfold-symmetric ring (or the corner of the octagon), there will naturally be three minima within the octagon while the other first-order neighbors lie outside of it. The configuration-space construction hence in all cases automatically selects the right number of minima to reproduce the lowest band.

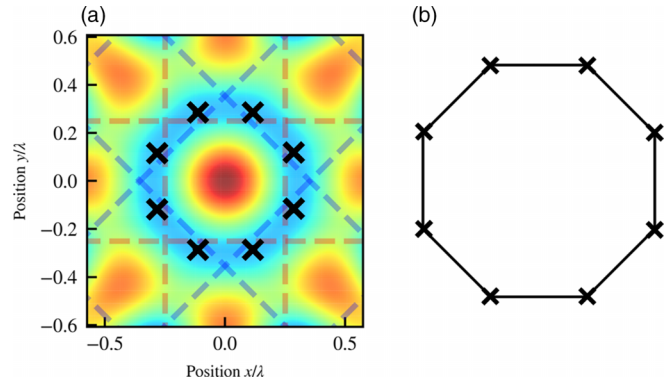

FIG. 20. Sites (crosses) located on the eight corners of the octagon (right) form an eightfold-symmetric ring, separated by shallow potential barriers. This constitutes one of the symmetry centers of the 8QC.

APPENDIX H: NEIGHBORS CLASSIFICATION AND TUNNELING AMPLITUDES

In contrast to for instance the regular square lattice, it is not possible to write an unambiguous definition for nearest neighbors in the 8QC based on real-space distances. In configuration space, however, nearest neighbors and higher-order neighbors can be defined rigorously, identically to what is done in the perpendicular space of discrete quasicrystals [49].

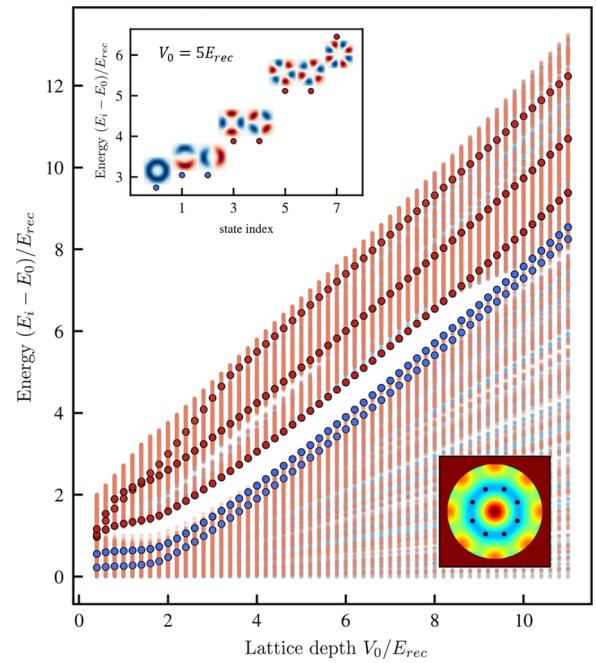

FIG. 21. Blue and red circled dots: energy spectrum of a ring containing eight minima (inset, lower right) obtained by exact diagonalization in continuum. Background: bulk energy spectrum of the 8QC from Fig. 3. The lowest three states of the ring contribute to the lowest band (blue circled dots), while the remaining higher-lying states are located within the higher bands (red circled dots). Upper left inset shows the energy spectrum and the eight lowest ring eigenstates for $V_0 = 5\,E_{\mathrm{rec}}$.

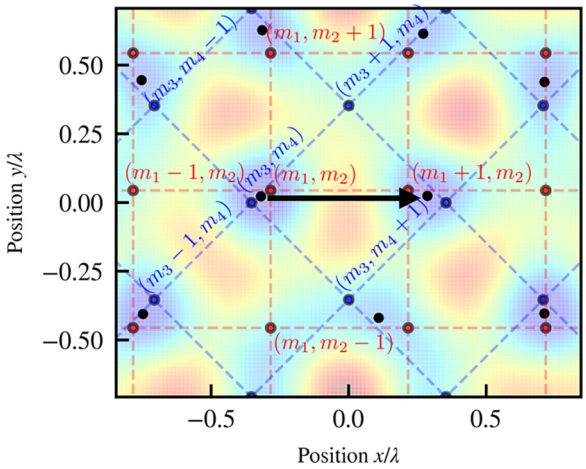

FIG. 22. Real-space neighbors (black dots) can be found around adjacent lattice sites of the square lattices (red and blue dots) underlying the 8QC. Red and blue labels indicate the indices of some of the sites adjacent to the (m_1, m_2) site of the XY lattice and (m_3, m_4) site of the D lattice. This illustrates that the nearest neighbor to the right (black arrow) is offset by $\{\Delta m_1, \Delta m_2, \Delta m_3, \Delta m_4\} = \{1, 0, 1, 1\}$ so that $\mathbf{\Phi}' - \mathbf{\Phi} = \tilde{\mathbf{e}}_x$.

We start by rewriting the expressions for $\mathbf{\Phi}_{\mathrm{XY}}$ and $\mathbf{\Phi}_{\mathrm{D}}$ [Eqs. (7) and (8)] by stating the modulo operation explicitly, and setting all ϕ_i to zero for simplicity:

$$\mathbf{\Phi}_{\mathrm{XY}}(x, y) = (x - m_1\, d)\mathbf{e}_x + (y - m_2\, d)\mathbf{e}_y, \tag{H1}$$

$$\mathbf{\Phi}_{\mathrm{D}}(x, y) = \left(\frac{x+y}{\sqrt{2}} - m_3\, d\right)\mathbf{e}_+ + \left(\frac{x-y}{\sqrt{2}} - m_4\, d\right)\mathbf{e}_-. \tag{H2}$$

Here, $m_1,\ m_2 \in \mathbb{Z}$ (which are functions of x and y) label the lattice sites of the XY lattice, while m_3 and m_4 label the sites of the D lattice (see Fig. 22), and the $\mathbf{e}_i$ with $i \in \{x, y, +, -\}$ are unit vectors along the four lattice directions in Fig. 2. In turn, we can re-write the expression for $\mathbf{\Phi} = \mathbf{\Phi}_{\mathrm{XY}} - \mathbf{\Phi}_{\mathrm{D}}$:

$$\mathbf{\Phi}(x, y) = d\left(-m_1 + \frac{m_3 + m_4}{\sqrt{2}}\right)\mathbf{e}_x + d\left(-m_2 + \frac{m_3 - m_4}{\sqrt{2}}\right)\mathbf{e}_y. \tag{H3}$$

As an aside, we note that this form also makes it apparent that the octagon is populated densely and uniformly, as the equidistribution theorem [68] ensures that the decimal part of sequences of the form $x_n = \alpha n$ with α irrational and n the sequence of natural numbers must be uniformly dense in the interval [0, 1[.

Let us now consider two neighboring sites of the 8QC that correspond to the integers $\{m_1, m_2, m_3, m_4\}$, $\{m_1', m_2', m_3', m_4'\}$ (see Fig. 22) and local displacements $\mathbf{\Phi}'$ and $\mathbf{\Phi}$. We can then rewrite the vector connecting $\mathbf{\Phi}'$ to $\mathbf{\Phi}$ as

$$\mathbf{\Phi}' - \mathbf{\Phi} = d\left(-\Delta m_1 + \frac{\Delta m_3 + \Delta m_4}{\sqrt{2}}\right)\mathbf{e}_x + d\left(-\Delta m_2 + \frac{\Delta m_3 - \Delta m_4}{\sqrt{2}}\right)\mathbf{e}_y \tag{H4}$$

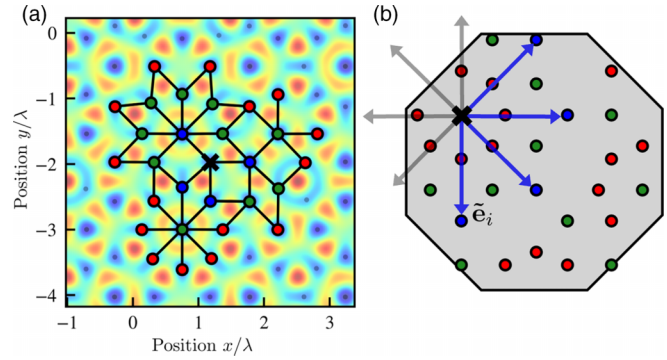

FIG. 23. First-, second-, and third-order neighbors of a given site (black cross) in real (a) and configuration (b) space constructed by $\mathbf{\Phi}' = \mathbf{\Phi} + \sum_i c_i\tilde{\mathbf{e}}_i$ with $c_i \in \mathbb{Z}$ and $\sum|c_i| = \{1, 2, 3\}$. (Blue) First-order neighbors. (Green) Second-order neighbors. (Red) Third-order neighbors. Black lines connect first-order neighbors.

with $\Delta m_i = m_i' - m_i$. In real space, nearest neighbors cannot be more than one unit cell of the XY and D lattices away, i.e., $|\Delta m_i| \in \{0, 1\}$.

This is clearly visible in Fig. 22. Here, the vector connecting the lattice site defined by $\{m_1, m_2, m_3, m_4\}$ to its right-hand neighbor defined by $\{m_1 + 1, m_2, m_3 + 1, m_4 + 1\}$, amounts to $\mathbf{\Phi}' - \mathbf{\Phi} = -\frac{d}{1+\sqrt{2}}\mathbf{e}_x$. Thanks to eightfold symmetry, the same reasoning can be applied in all eight directions, leading to

$$\tilde{\mathbf{e}}_i \in \pm\frac{d}{1+\sqrt{2}}\{\mathbf{e}_x, \mathbf{e}_y, \mathbf{e}_+, \mathbf{e}_-\}. \tag{H5}$$

Figure 23 shows that vectors of the form $\mathbf{\Phi} + \tilde{\mathbf{e}}_i$, if they lie within the octagon, do indeed correspond to close neighbors in real space and we accordingly define *first-order* neighbors as sites separated by the vectors $\tilde{\mathbf{e}}_i$ in configuration space. This is identical to the definition of first-order neighbors in the perpendicular space of eightfold discrete quasicrystals [49].

In turn, we can define the nth-order neighbors of a given site as the set of surrounding sites that lie on the octagon and are connected through the sum of at least n vectors $\tilde{\mathbf{e}}_i$, i.e., $\mathbf{\Phi}' = \mathbf{\Phi} + \sum_i c_i\tilde{\mathbf{e}}_i$ with $c_i \in \mathbb{Z}$ and $\sum|c_i| = n$. We refer to the vector connecting nth-order neighbors as $\tilde{\mathbf{e}}_i^n$. Figure 23 shows an example of first-, second-, and third-order neighbors. Using this definition, first-order neighbors sit on the edges of the square and rhombuses of the corresponding Ammann-Beenker tiling [43], while second-order neighbors are separated via two edges. Pairs of sites along the short diagonals of the rhombuses are therefore second-order neighbors even though they lie close to each other in real space and give rise to significant (negative) tunneling amplitudes.

Similarly to the smooth surfaces formed by the onsite energy $\epsilon(\mathbf{\Phi})$ and the onsite interaction $U(\mathbf{\Phi})$, the tunneling amplitudes connecting two sites $\mathbf{\Phi}, \mathbf{\Phi}'$ can be written as a function $J(\mathbf{\Phi}, \mathbf{\Phi}')$ in configuration space. If we restrict ourselves to nth-order neighbors, we know that $\mathbf{\Phi} - \mathbf{\Phi}' = \mathbf{e}_k^n$. Therefore, for each $\mathbf{e}_k^n$ we define a smooth function $J_{\mathbf{e}_k^n}(\mathbf{\Phi}) \equiv J(\mathbf{\Phi}, \mathbf{\Phi} + \mathbf{e}_k^n)$ and plot a cut through this function in Fig. 24.

Finally, Fig. 25 shows the distributions and mean values for the total tunneling amplitudes connecting first-, second-, and third-order neighbors. While first- and second-order tunneling

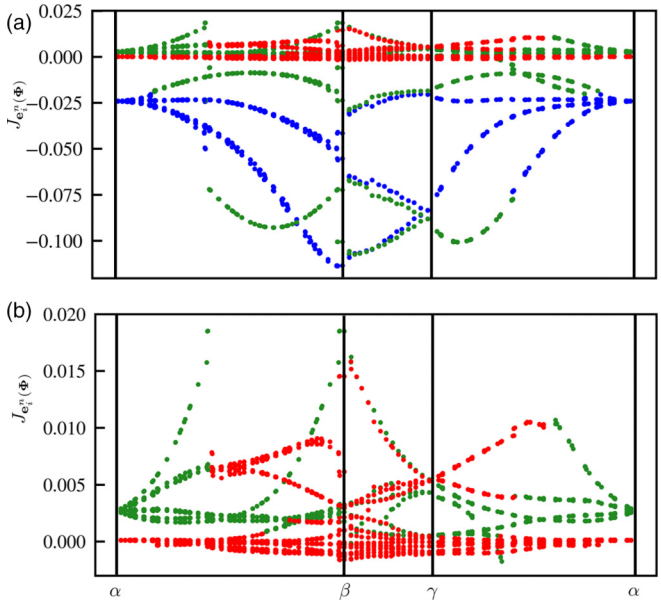

FIG. 24. Tunneling amplitudes $J_{\mathbf{e}_k^n}(\mathbf{\Phi}_i) \equiv J(\mathbf{\Phi}, \mathbf{\Phi} + \mathbf{e}_k^n)$ for $V_0 = 2.5\, E_{\mathrm{rec}}$ along a cut through configuration space (see Fig. 11 for definition of α, β, and γ points). (Blue) First-order neighbors. (Green) Second-order neighbors. (Red) Third-order neighbors. First-order neighbors are always characterized by negative J. (b) Same as (a) but zoomed in on positive tunneling amplitudes.

can have comparable amplitudes, tunneling amplitudes connecting third-order neighbors are significantly weaker for all lattice depths. This also highlights that even though the Ammann-Beenker tiling is bipartite, the 8QC is not.

APPENDIX I: RELATION BETWEEN CONFIGURATION AND PERPENDICULAR SPACES OF THE 8QC

Here we show that the 8QC configuration space introduced in this work directly corresponds to the perpendicular space

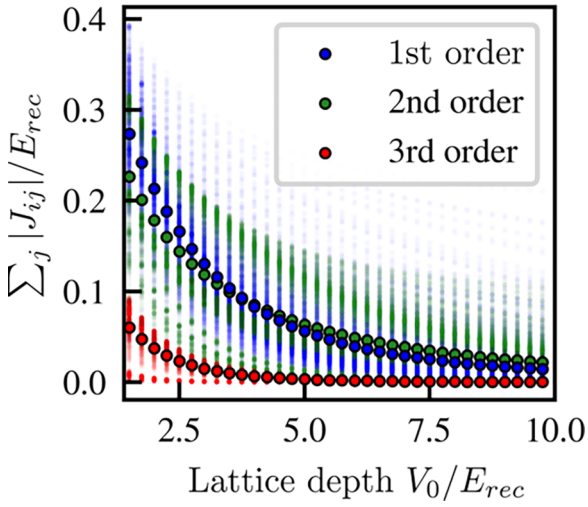

FIG. 25. Distributions of first-, second-, and third-order total tunneling amplitudes versus lattice depth. Circled dots show the mean values of the distributions. (Blue) First-order neighbors. (Green) Second-order neighbors. (Red) Third-order neighbors.

of discrete octagonal quasicrystals. Both form a densely and uniformly populated octagon, where lattice sites are ordered in terms of their local surroundings.

Let us first introduce the perpendicular space of discrete octagonal quasicrystals. These quasicrystals can be obtained using a cut-and-project method at an irrational angle of a four-dimensional (4D) hypercubic lattice [42,67]

Let $\{\mathbf{e}_1, \mathbf{e}_2, \mathbf{e}_3, \mathbf{e}_4\}$ be a basis of $\mathbb{R}^4$, and define the hypercubic lattice as the set of their integer combinations. We then project the 4D hypercubic lattice into two orthogonal subspaces: the "physical space" and "perpendicular" space, using the projection maps π and $\pi^\perp$, respectively. These are defined as

$$\pi = \begin{pmatrix} 1 & 0 & \frac{1}{\sqrt{2}} & \frac{1}{\sqrt{2}} \\ 0 & 1 & \frac{-1}{\sqrt{2}} & \frac{1}{\sqrt{2}} \end{pmatrix}, \tag{I1}$$

$$\pi^\perp = \begin{pmatrix} -1 & 0 & \frac{1}{\sqrt{2}} & \frac{1}{\sqrt{2}} \\ 0 & 1 & \frac{1}{\sqrt{2}} & \frac{-1}{\sqrt{2}} \end{pmatrix}. \tag{I2}$$

The 2D quasicrystalline lattice can then be obtained as the set of physical space positions of the hypercubic lattice sites whose perpendicular space image lies within a certain "acceptance window." A common choice for this window is to set it equal to the perpendicular space image of the hypercubic Wigner-Seitz cell.

Let us now turn the the configuration space of the 8QC. The optical potential can be obtained as an irrational cut of a four-dimensional hypercubic optical potential (where we fixed all phases ϕ_i to 0 for simplicity)

$$V_{4\mathrm{D}}(x_1, x_2, x_3, x_4) = V_0 \sum_{i=1}^{4} \sin^2\left(\frac{2\pi}{\lambda} x_i\right) \tag{I3}$$

by setting $x_3 = \frac{x_1+x_2}{\sqrt{2}}$ and $x_3 = \frac{x_1-x_2}{\sqrt{2}}$.

In turn, we can rewrite the configuration-space coordinates in four dimensions:

$$\mathbf{\Phi} = \mathbf{\Phi}_{\mathrm{XY}} - \mathbf{\Phi}_{\mathrm{D}} \tag{I4}$$

with

$$\mathbf{\Phi}_{\mathrm{XY}} = \begin{pmatrix} x_1 \bmod d \\ x_2 \bmod d \end{pmatrix} = \begin{pmatrix} \tilde{x}_1 \\ \tilde{x}_2 \end{pmatrix}, \tag{I5}$$

$$\mathbf{\Phi}_{\mathrm{D}} = \frac{1}{\sqrt{2}} \begin{pmatrix} x_3 \bmod d + x_4 \bmod d \\ x_3 \bmod d - x_4 \bmod d \end{pmatrix} = \frac{1}{\sqrt{2}} \begin{pmatrix} \tilde{x}_3 + \tilde{x}_4 \\ \tilde{x}_3 - \tilde{x}_4 \end{pmatrix}. \tag{I6}$$

This directly leads to

$$\mathbf{\Phi} = \begin{pmatrix} \tilde{x}_1 - \frac{\tilde{x}_3+\tilde{x}_4}{\sqrt{2}} \\ \tilde{x}_2 - \frac{\tilde{x}_3-\tilde{x}_4}{\sqrt{2}} \end{pmatrix} = \begin{pmatrix} 1 & 0 & \frac{-1}{\sqrt{2}} & \frac{-1}{\sqrt{2}} \\ 0 & 1 & \frac{-1}{\sqrt{2}} & \frac{1}{\sqrt{2}} \end{pmatrix} \begin{pmatrix} \tilde{x}_1 \\ \tilde{x}_2 \\ \tilde{x}_3 \\ \tilde{x}_4 \end{pmatrix}, \tag{I7}$$

which shows that, up to a sign change, the 8QC configuration space is identical to the perpendicular space projection map $\pi^\perp$ [Eq. (I2)].

[1] M. Senechal, *Quasicrystals and Geometry* (Cambridge University Press, Cambridge, 1995).

[2] L.-J. Lang, X. Cai, and S. Chen, Edge States and Topological Phases in One-Dimensional Optical Superlattices, Phys. Rev. Lett. **108**, 220401 (2012).

[3] Y. E. Kraus and O. Zilberberg, Topological Equivalence between the Fibonacci Quasicrystal and the Harper Model, Phys. Rev. Lett. **109**, 116404 (2012).

[4] Y. E. Kraus, Y. Lahini, Z. Ringel, M. Verbin, and O. Zilberberg, Topological States and Adiabatic Pumping in Quasicrystals, Phys. Rev. Lett. **109**, 106402 (2012).

[5] Y. E. Kraus, Z. Ringel, and O. Zilberberg, Four-Dimensional Quantum Hall Effect in a Two-Dimensional Quasicrystal, Phys. Rev. Lett. **111**, 226401 (2013).

[6] F. Matsuda, M. Tezuka, and N. Kawakami, Topological properties of ultracold bosons in one-dimensional quasiperiodic optical lattice, J. Phys. Soc. Jpn. **83**, 083707 (2014).

[7] J. Puig, in *Cantor Spectrum for Quasi-Periodic Schrödinger Operators*, edited by J. Asch and A. Joye (Springer, Berlin, 2006), pp. 79–91.

[8] P. W. Anderson, Absence of diffusion in certain random lattices, Phys. Rev. **109**, 1492 (1958).

[9] E. Abrahams, P. W. Anderson, D. C. Licciardello, and T. V. Ramakrishnan, Scaling Theory of Localization: Absence of Quantum Diffusion in Two Dimensions, Phys. Rev. Lett. **42**, 673 (1979).

[10] S. Aubry and G. André, in *Analyticity Breaking and Anderson Localization in Incommensurate Lattices* (Adam Hilger, Bristol, 1980), pp. 133–164.

[11] R. B. Diener, G. A. Georgakis, J. Zhong, M. Raizen, and Q. Niu, Transition between extended and localized states in a one-dimensional incommensurate optical lattice, Phys. Rev. A **64**, 033416 (2001).

[12] J. Biddle, B. Wang, D. J. Priour, and S. Das Sarma, Localization in one-dimensional incommensurate lattices beyond the Aubry-André model, Phys. Rev. A **80**, 021603(R) (2009).

[13] J. Biddle, D. J. Priour, B. Wang, and S. Das Sarma, Localization in one-dimensional lattices with non-nearest-neighbor hopping: Generalized anderson and Aubry-André models, Phys. Rev. B **83**, 075105 (2011).

[14] S. Ganeshan, J. H. Pixley, and S. Das Sarma, Nearest Neighbor Tight Binding Models with an Exact Mobility Edge in One Dimension, Phys. Rev. Lett. **114**, 146601 (2015).

[15] D. A. Abanin and Z. Papić, Recent progress in many-body localization, Ann. Phys. **529**, 1700169 (2017).

[16] T. Vojta, Disorder in quantum many-body systems, Annu. Rev. Condens. Matter Phys. **10**, 233 (2019).

[17] R. Nandkishore and D. A. Huse, Many-body localization and thermalization in quantum statistical mechanics, Annu. Rev. Condens. Matter Phys. **6**, 15 (2015).

[18] E. Altman and R. Vosk, Universal dynamics and renormalization in many-body-localized systems, Annu. Rev. Condens. Matter Phys. **6**, 383 (2015).

[19] D. A. Abanin, E. Altman, I. Bloch, and M. Serbyn, Colloquium: Many-body localization, thermalization, and entanglement, Rev. Mod. Phys. **91**, 021001 (2019).

[20] V. Khemani, D. N. Sheng, and D. A. Huse, Two Universality Classes for the Many-Body Localization Transition, Phys. Rev. Lett. **119**, 075702 (2017).

[21] W. De Roeck and F. Huveneers, Stability and instability towards delocalization in many-body localization systems, Phys. Rev. B **95**, 155129 (2017).

[22] N. Marzari, A. A. Mostofi, J. R. Yates, I. Souza, and D. Vanderbilt, Maximally localized wannier functions: Theory and applications, Rev. Mod. Phys. **84**, 1419 (2012).

[23] S. Q. Zhou and D. M. Ceperley, Construction of localized wave functions for a disordered optical lattice and analysis of the resulting hubbard model parameters, Phys. Rev. A **81**, 013402 (2010).

[24] J. Zhu, Z. Chen, and B. Wu, Construction of maximally localized wannier functions, Front. Phys. **12**, 127102 (2017).

[25] F. Liu, S. Ghosh, and Y. D. Chong, Localization and adiabatic pumping in a generalized Aubry-André-Harper model, Phys. Rev. B **91**, 014108 (2015).

[26] A. Szabo and U. Schneider, Non-power-law universality in one-dimensional quasicrystals, Phys. Rev. B **98**, 134201 (2018).

[27] A. Geißler and G. Pupillo, Mobility edge of the two-dimensional bose-hubbard model, Phys. Rev. Res. **2**, 042037(R) (2020).

[28] K. Viebahn, M. Sbroscia, E. Carter, J.-C. Yu, and U. Schneider, Matter-Wave Diffraction from a Quasicrystalline Optical Lattice, Phys. Rev. Lett. **122**, 110404 (2019).

[29] M. Sbroscia, K. Viebahn, E. Carter, J.-C. Yu, A. Gaunt, and U. Schneider, Observing Localization in a 2D Quasicrystalline Optical Lattice, Phys. Rev. Lett. **125**, 200604 (2020).

[30] D. Bennett and B. Remez, On electrically tunable stacking domains and ferroelectricity in moiré superlattices, npj 2D Mater. Appl. **6**, 7 (2022).

[31] S. Carr, D. Massatt, S. B. Torrisi, P. Cazeaux, M. Luskin, and E. Kaxiras, Relaxation and domain formation in incommensurate two-dimensional heterostructures, Phys. Rev. B **98**, 224102 (2018).

[32] D. Massatt, M. Luskin, and C. Ortner, Electronic density of states for incommensurate layers, Multiscale Model. Simul. **15**, 476 (2017).

[33] G. Rai, H. Schlomer, C. Matsumura, S. Haas, and A. Jagannathan, Bulk topological signatures of a quasicrystal, Phys. Rev. B **104**, 184202 (2021).

[34] A. Jagannathan, Quasiperiodic heisenberg antiferromagnets in two dimensions, Eur. Phys. J. B **85**, 68 (2012).

[35] R. Ghadimi, T. Sugimoto, and T. Tohyama, Mean-field study of the bose-hubbard model in the penrose lattice, Phys. Rev. B **102**, 224201 (2020).

[36] A. Szallas and A. Jagannathan, Spin waves and local magnetizations on the penrose tiling, Phys. Rev. B **77**, 104427 (2008).

[37] M. Mirzhalilov and M. O. Oktel, Perpendicular space accounting of localized states in a quasicrystal, Phys. Rev. B **102**, 064213 (2020).

[38] O. Dutta, M. Gajda, P. Hauke, M. Lewenstein, D.-S. Lühmann, B. A. Malomed, T. Sowiński, and J. Zakrzewski, Non-standard hubbard models in optical lattices: A review, Rep. Prog. Phys. **78**, 066001 (2015).

[39] *On the Nonorthogonality Problem*, edited by P.-O. Löwdin (Academic Press, New York, 1970), Vol. 5, pp. 185–199.

[40] J. G. Aiken, J. A. Erdos, and J. A. Goldstein, On Löwdin orthogonalization, Int. J. Quantum Chem. **18**, 1101 (1980).

[41] C. Lanczos, An iteration method for the solution of the eigenvalue problem of linear differential and integral operators, J. Res. Natl. Bur. Stand. **45**, 255 (1950).

[42] A. Jagannathan and M. Duneau, An eightfold optical quasicrystal with cold atoms, Europhys. Lett. **104**, 66003 (2013).
[43] N. Macé, A. Jagannathan, and M. Duneau, Quantum simulation of a 2D quasicrystal with cold atoms, Crystals **6**, 124 (2016).
[44] O. Zilberberg, Topology in quasicrystals, Opt. Mater. Express **11**, 1143 (2021).
[45] A. E. Niederle and H. Rieger, Bosons in a two-dimensional bichromatic quasiperiodic potential: Analysis of the disorder in the Bose-Hubbard parameters and phase diagrams, Phys. Rev. A **91**, 043632 (2015).
[46] A. Szabo and U. Schneider, Mixed spectra and partially extended states in a two-dimensional quasiperiodic model, Phys. Rev. B **101**, 014205 (2020).
[47] R. Gautier, H. Yao, and L. Sanchez-Palencia, Strongly Interacting Bosons in a Two-Dimensional Quasicrystal Lattice, Phys. Rev. Lett. **126**, 110401 (2021).
[48] J.-Y. Choi, S. Hild, J. Zeiher, P. Schauß, A. Rubio-Abadal, T. Yefsah, V. Khemani, D. A. Huse, I. Bloch, and C. Gross, Exploring the many-body localization transition in two dimensions, Science **352**, 1547 (2016).
[49] M. O. Oktel, Strictly localized states in the octagonal ammann-beenker quasicrystal, Phys. Rev. B **104**, 014204 (2021).
[50] S. Spurrier and N. R. Cooper, Semiclassical dynamics, berry curvature, and spiral holonomy in optical quasicrystals, Phys. Rev. A **97**, 043603 (2018).
[51] U. Agrawal, R. Vasseur, and S. Gopalakrishnan, Quasiperiodic many-body localization transition in dimension $d > 1$, Phys. Rev. B **106**, 094206 (2022).
[52] L. Pollet, A review of monte carlo simulations for the bose-hubbard model with diagonal disorder, C. R. Phys. **14**, 712 (2013).
[53] T. Giamarchi and H. J. Schulz, Anderson localization and interactions in one-dimensional metals, Phys. Rev. B **37**, 325 (1988).
[54] M. P. A. Fisher, P. B. Weichman, G. Grinstein, and D. S. Fisher, Boson localization and the superfluid-insulator transition, Phys. Rev. B **40**, 546 (1989).
[55] J. Kisker and H. Rieger, Bose-glass and mott-insulator phase in the disordered boson hubbard model, Phys. Rev. B **55**, R11981 (1997).
[56] P. Hitchcock and E. S. Sørensen, Bose-glass to superfluid transition in the three-dimensional bose-hubbard model, Phys. Rev. B **73**, 174523 (2006).
[57] P. Sengupta and S. Haas, Quantum Glass Phases in the Disordered Bose-Hubbard Model, Phys. Rev. Lett. **99**, 050403 (2007).
[58] G. Roux, T. Barthel, I. P. McCulloch, C. Kollath, U. Schollwöck, and T. Giamarchi, Quasiperiodic bose-hubbard model and localization in one-dimensional cold atomic gases, Phys. Rev. A **78**, 023628 (2008).
[59] L. Pollet, N. V. Prokof'ev, B. V. Svistunov, and M. Troyer, Absence of a Direct Superfluid to Mott Insulator Transition in Disordered Bose Systems, Phys. Rev. Lett. **103**, 140402 (2009).
[60] S. G. Soyler, M. Kiselev, N. V. Prokof'ev, and B. V. Svistunov, Phase Diagram of the Commensurate Two-Dimensional Disordered Bose-Hubbard Model, Phys. Rev. Lett. **107**, 185301 (2011).
[61] D. Johnstone, P. Öhberg, and C. W. Duncan, Mean-field phases of an ultracold gas in a quasicrystalline potential, Phys. Rev. A **100**, 053609 (2019).
[62] D. Johnstone, P. Öhberg, and C. W. Duncan, The mean-field bose glass in quasicrystalline systems, J. Phys. A: Math. Theor. **54**, 395001 (2021).
[63] M. Ciardi, T. Macri, and F. Cinti, Finite-temperature phases of trapped bosons in a two-dimensional quasiperiodic potential, Phys. Rev. A **105**, L011301 (2022).
[64] https://doi.org/10.17863/CAM.95664.
[65] G. Mazzarella, S. M. Giampaolo, and F. Illuminati, Extended bose hubbard model of interacting bosonic atoms in optical lattices: From superfluidity to density waves, Phys. Rev. A **73**, 013625 (2006).
[66] T. Sowinski, O. Dutta, P. Hauke, L. Tagliacozzo, and M. Lewenstein, Dipolar Molecules in Optical Lattices, Phys. Rev. Lett. **108**, 115301 (2012).
[67] J. Jeon and S. Lee, Discovery of new quasicrystals from translation of hypercubic lattice, arXiv:2112.14783.
[68] A. Zorzi, An elementary proof for the equidistribution theorem, Math. Intell. **37**, 1 (2015).